Investigating Isomer Release in ^{121}Sb Through Low-Energy Coulomb Excitation

Gil Goodman

A thesis submitted for the degree of
Bachelor of Science (Honours) in Physics at
The Australian National University

October 2024

Declaration

This thesis is an account of research undertaken between February 2024 and October 2024 at the Research School of Physics, the Australian National University, Canberra, Australia.

Except where acknowledged in the customary manner, the material presented in this thesis is, to the best of my knowledge, original and has not been submitted in whole or part for a degree at any other university.

Gil Goodman

October 2024

Abstract

Long-lived nuclear excited states known as isomers have been identified as a potential method of energy storage. The atomic nuclei would store energy while suspended in the isomer, which is then de-populated to release the energy for use. A release mechanism is needed to depopulate the isomer on demand. One potential mechanism is Coulomb excitation. This thesis reports on an experiment to verify the assumptions of Coulomb excitation at low excitation energies. Coulomb-excitation measurements of the low-lying excited states of ^{121}Sb have been made to determine the $B(E2)$ values of the low-energy transitions and compare them to literature. The mean lifetimes of the excited states have also been calculated from the measured transition strengths. The present $B(E2)$ values vary in their agreement, with some values agreeing within uncertainty of the literature values and others being in disagreement with the literature. Most of the calculated mean lifetimes deviated from the literature values. The results show promise but further constraining of the data would improve the accuracy of the results.

Preface

This thesis involved collaborative work and used equipment and codes developed by others. This preface outlines my contributions and the contribution of others.

The experimental setup of the CAESAR array was performed by me, my supervisors AJ Mitchell and Ben Coombes and PhD candidate Jack Woodside, along with assistance from other members of the research group. The selection of the beam species was performed by me in discussion with AJ and Ben.

The ^{121}Sb target and copper backing used in the experiment were manufactured by Andrew Stuchbery at ANU.

The ANU 14UD accelerator is operated 24 hours a day and operating it is taken in shifts. The rostered shifts included many members of the research group and technical support throughout the experiments was provided by Peter Lindarkis and Nikolai Lobanov.

A number of pre-existing computer codes were used in this project. The code **CaesarSort**, developed by the research group, was used for sorting the raw experimental data. The code **strop3**, developed by Andrew Stuchbery, was used to calculate the energy loss in the target. **GetBetas**, developed by Jack Woodside, was used to perform Doppler corrections on the γ-ray energy spectra. I used the Coulomb-excitation code **Gosia** and the input files were modified from existing files made by Martha Reece and Jack. The application of the codes to the data analysis and interpretation were performed in discussion with AJ, Ben and Jack.

Acknowledgements

An Honours project is ultimately a collective effort and I would like to thank everyone both within the Department of Nuclear Physics and Accelerator Applications (NPAA) and outside it who helped me complete my project.

Firstly, thank you to my supervisors Dr AJ Mitchell and Dr Ben Coombes for supporting me during my project and for answering the many questions I had throughout. I have learnt so much over the course of this year under your supervision. Also thank you to Professor Andrew Stuchbery and Professor Greg Lane for sharing their knowledge of nuclear physics and experience in analysing experimental data.

I would like to thank the HIAF technical staff for keeping the accelerator running during my experiments. Because of your efforts, my and many other experiments are able to run smoothly. I would also like to thank everyone who gave up their time to do shifts in the accelerator during my experiment: AJ Mitchell, Abijith Gopakumar, Aditya Babu, Ben Coombes, Ferdos Dastgiri, Greg Lane, Hanaa Alshammari, Jack Woodside, Lachie McKie, Nathan Spinks, Riakako Kono, Ryan Leonard, Tom Perissinotto and Victoria Bashu.

Thank you to all my friends and family for their support during the year and to my fellow honours students for helping to share the stress during the many busy periods we went through. Thank you to the other students in the Department of Nuclear Physics for making lunch conversations something to look forward to every day and for sharing your experiences on running experiments. Thank you to my housemates Alex and Harry for their understanding during a very stressful period of my studies.

Finally, thank you to Jack Woodside spending time helping with all of my programming troubles, of which there were many. Your programs helped speed up the analysis and you always put the extra effort in to make any program you wrote intuitive to use. You were always helping me find errors in my code and **Gosia** input files. My project would have been a lot more difficult without your countless hours of assistance.

Contents

Chapter 1

Introduction

Energy-storage technology is a critical aspect of the modern world. A key feature of energy-storage devices is their ability to reliably store energy for extended periods of time and then safely release it on demand. For example, chemical batteries store energy as chemical potential energy. When an electric potential is applied, the chemical potential energy is converted into electrical energy for use. Energy storage can also be performed using atomic nuclei.

Nuclei gain excess energy when they are promoted to excited states and release the energy as they relax to their ground state. Nuclear-based energy-storage devices have a specific energy on the order of $10^{12}\,\mathrm{J\,kg^{-1}}$, which is orders of magnitude larger than chemical battery designs such as lead-acid batteries which have specific energies on the order of $10^{5}\,\mathrm{J\,kg^{-1}}$ [1, 2]. Utilising nuclear processes in energy storage could lead to significant increases in energy storage capacity.

There are a range of methods to store energy using nuclear processes. One approach is to use highly unstable nuclei known as radioisotopes. Atomic nuclei have a discrepancy in their measured masses as the mass energy of the nucleus is less than the mass energy calculated from the atomic mass number, A, of the nucleus. This difference is known as the mass excess and the stability of a nucleus is related to this quantity [3]. The mass excess of isobars, nuclei of different elements with the same A, can be represented by a quadratic function of proton number Z. The vertex of the quadratic represents the most stable nucleus for a given A, and stability decreases as Z is varied away from the vertex [4, 5]. Radioisotopes have larger mass excesses than their neighbouring isobars and undergo β decay to reach a stable Z-number and decrease the mass excess. Radioisotopes with large Z and A also undergo α decay to reduce their internal energy due to Coulomb repulsion between protons. In both cases, these nuclei emit decay products and undergo

transformations to reach a more stable state. A radioisotope-based energy-storage device captures the energy of the decay products as heat and converts it into electrical energy [1]. While able to store large quantities of energy, radioisotopes have significant limitations. Primarily, the radioactive decay rate cannot be controlled, so the power output is unable adapt to varying energy demands. Another drawback of radioisotopes is that the emitted radiation poses a health risk, increasing the difficulty of operating and transporting the energy-storage device [6, 7].

An alternative to radioisotopes is to store energy by suspending the nucleus in an excited state and then de-exciting it to access the energy. Unlike radioisotope decay, nuclear de-excitation releases less-harmful γ rays, and the energy output could potentially be controlled by stimulating the nuclei on demand. An obstacle to this approach is that nuclear excited states typically have lifetimes on the order of femtoseconds, which is too short of a time scale for practical energy-storage applications. However, a potential solution is to use cases of excited states that exist for longer periods of time, known as isomers.

The discovery of nuclear isomers was credited to Otto Hahn in 1921. While investigating the β decay of ^{234}Th to ^{234}Pa, Hahn noticed that there was an activity between the decay of ^{234}Th and ^{234}Pa entering its ground state [8]. This implied the existence of a long-lived nuclear excited state, which generated considerable interest as it was assumed all nuclear excited states had lifetimes of the order 10^{-13} s [8, 9]. Further work in the 1930s showed that an electromagnetic decay transition of low energy and high angular momentum would have a longer decay half-life [9]. This demonstrated that long-lived formed where the nucleus was inhibited from decaying to lower-energy states. During the 1950s, more isomers were discovered and were being used to develop models for deformed nuclei. For example, research into the rotational motion of nuclei was related to the discovery of high-spin isomers [10]. Isomers now form part of the larger research into metastable nuclear states, which are excited states that exhibit properties of stable states [11].

Through its long lifetime, the nucleus can be held in the isomer for extended periods of time and potentially be made to release the energy on demand. However, the stability of isomers presents an obstacle for accessing the stored energy. Isomers exhibit exponential

decay rates, where the rate of energy release is governed by the lifetime of the isomer. As an isomer used for energy storage would need to have a minimum lifetime of months and therefore a relatively small decay probability, this is an impractical method of releasing the energy. An alternative approach to harness the energy of an isomer is through excitation to an intermediate depletion state, as depicted in Fig. 1.1. Population transitions from isomers are not inhibited, so nuclei can be released from isomers by excitation to a higher-energy state. If the depletion state is not an isomer, the nucleus will rapidly decay to the ground state, releasing the stored energy. Therefore, an approach to isomer energy-storage is to use a mechanism that can excite the nucleus to a depletion state.

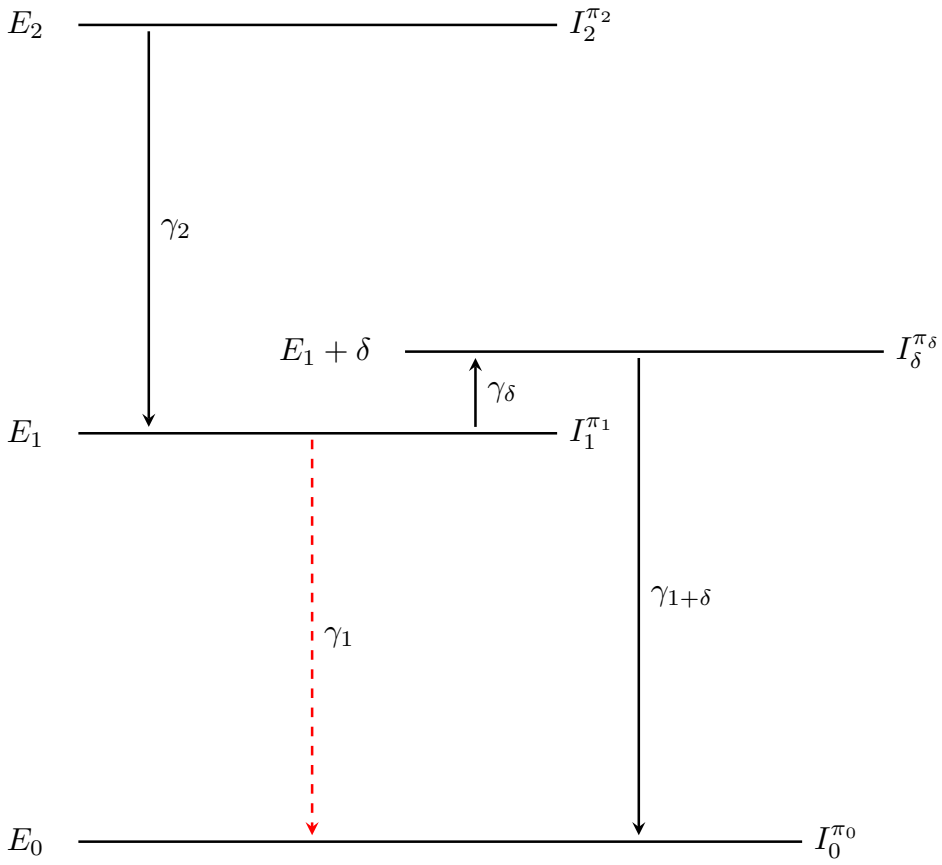

Figure 1.1: An example nuclear level scheme showing a nuclear depletion path. The I_1 state is populated by the γ_2 transition from the I_2 state. The γ_1 transition is inhibited which results in the I_1 state having a long mean lifetime. The energy may be released faster if the nucleus can be promoted to the I_δ state through a γ_δ excitation, where it then rapidly decays to the ground state.

A method that has been discovered for isomer de-excitation is nuclear excitation by electron capture (NEEC). When electrons are captured by ions, a resonance excitation

can occur through the electromagnetic interaction between the captured electrons and the nucleus. NEEC facilitates this resonance to excite a nucleus out of an isomer and into a depletion state, where it then decays and releases energy. NEEC is performed by accelerating an ion in an isomeric state to velocities above 10% of the speed of light and directing it into a target medium. The valence electrons are stripped off when the ions pass through the target medium, giving the ion a high positive charge. Successive collisions with atoms in the target medium reduce the velocity of the ion. The lower velocity and positive charge increases the probability of the ion capturing free electrons to fill its valence shell. When electrons are captured, a resonance excitation is produced that excites the nucleus out of the isomer [12]. NEEC was first theorised in 1976 and experimentally demonstrated in 2018 using ^{93}Mo [12]. However, the theoretical and experimental results are yet to fully align due to an underestimation of the experimental backgrounds [13].

Another approach is to use Coulomb excitation as an energy release mechanism. Coulomb excitation is the process of bombarding a projectile nucleus onto a target nucleus, exciting both nuclei through an electromagnetic interaction. The energy of the projectile is selected such that the electromagnetic interaction is dominant while the nuclear strong force interaction is minimised to prevent undesirable nuclear effects such as fusion from occurring. Coulomb excitation would provide the energy to excite the nucleus from an isomeric state to a depletion state so it can then decay to the ground state. While the theory indicates that Coulomb excitation will work in the low-energy range, it has yet to be experimentally verified at energies below 100 keV.

The aim of this thesis is to investigate the theoretical assumptions of Coulomb excitation at low energy. Antimony-121 presents a suitable target for testing low-energy Coulomb excitation, as it has an isomer in the low-energy range. By Coulomb exciting ^{121}Sb nuclei and measuring the γ-ray yields, the behaviour of Coulomb excitation at low energy can be compared to the theoretical predictions.

Chapter 2

Background

2.1 Nuclear Structure

Atomic nuclei are comprised of positively-charged protons and neutral neutrons. The nucleus has a proton number Z, also representing its charge, a neutron number N and an atomic mass number A, which is equal to the sum of Z and N. The protons and neutrons, collectively known as nucleons, are held together by the nuclear strong force acting over distances on the order of femtometres. The strong-force interactions between the individual nucleons are often described with a mean-field potential [14]. As the protons have a positive charge, there is also a long-range Coulomb potential from the repulsive electromagnetic force between the protons. The nuclear and Coulomb potentials combine to form an attractive central potential in the nucleus surrounded by a repulsive Coulomb force that approaching nuclei have to overcome to reach the central potential.

2.1.1 Nuclear Shell Model

The nuclear shell model is based on the independent motion of the particles within a spherical mean-field attractive potential [15]. The attractive potential can be modelled by a Woods-Saxon form. Solutions of the three-dimensional Schrödinger equation using a Woods-Saxon phenomenological potential with an additional spin-orbit term, reproduce the occupation numbers of the closed shells observed in experimental data. Other spherical potentials, such as the Harmonic Oscillator and infinite well, are not suitable as infinite energy must be supplied to remove a nucleon from the potential in those models [14]. However, they do possess analytical solutions and provide a useful tool in some

situations. The Woods-Saxon potential is expressed as [14]

$$V_{\mathrm{WS}}(r) = \frac{-V_0}{1 + \exp\left(\frac{r - R_0}{a}\right)}, \tag{2.1}$$

where V_0 is the amplitude of the potential, r is the distance from the nucleus, R_0 is the mean radius expressed as

$$R_0 = r_0 A^{\frac{1}{3}}, \tag{2.2}$$

where $r_0 = 1.2\text{-}1.25\,\mathrm{fm}$, and a is the surface diffuseness. The Coulomb potential component of the shell model is represented as

$$V_C(r) = \begin{cases} \frac{Z_p Z_t e^2}{R_c}\left(\frac{3R_c^2 - r^2}{2R_c^2}\right) & r \leq R_c \\ \frac{Z_p Z_t e^2}{r} & r > R_c \end{cases} \tag{2.3}$$

where R_c is the sum of the nuclear radii. The piecewise form is to account for the uniform sphere approximation, where the Coulomb potential is a point charge at large r and a uniform sphere at small r.

The combination of the Coulomb and Wood-Saxon potentials produces a total nuclear potential dependent on the distance between the nuclei, as depicted in Fig. 2.1.

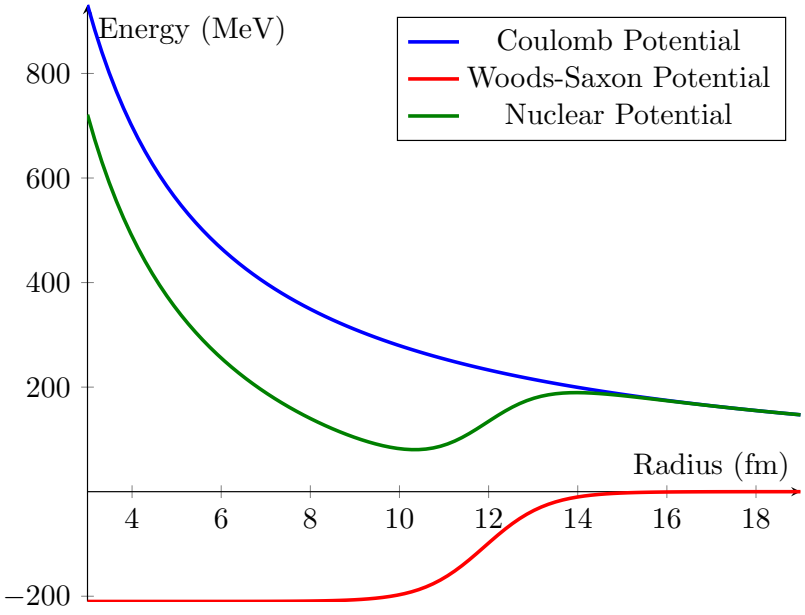

Figure 2.1: The potential experienced by one nucleus approaching another nucleus. The contributions from the Coulomb and Woods-Saxon potentials are included. The Coulomb potential is assumed to be a point charge.

The nuclear orbits correspond to potential energies that are eigenvalues of the Schrödinger equation. The largest energy gaps between orbits represent the 'magic' numbers of protons or neutrons. Nuclei with magic numbers of protons and/or neutrons are more stable. The magic numbers were found from examination of experimental data, such as low neutron absorption cross-sections for specific neutron numbers and elements with a greater amount of stable isotopes [16]. The magic numbers were determined to be $\{Z \text{ or } N = 2, 8, 20, 28, 50, 82, 126\}$, though 126 is unconfirmed for Z [17].

The Woods-Saxon potential reproduced the first three magic numbers but contradicted experimental evidence as more nucleons were added. The divergence between theory and experiment was corrected by the work of Maria Goeppert Mayer, who introduced a spin-orbit coupling component to the nuclear potential [17]. The spin-orbit potential V_{so} represents the force that interacts with the orbital angular momentum and spin of the nucleons. When the spin-orbit correction term was included in the shell model, it reproduced the experimental magic numbers. The current iteration of the shell model, illustrated in Fig. 2.2, is highly accurate at predicting the behaviour of nuclei near closed shells [15].

Spin and Parity

Each nucleon has an associated orbital angular momentum and spin, represented by the quantum numbers l and s, respectively, which arise from the occupation of levels of the nuclear potential. The sign of s represents the orientation of the spin of a nucleon. The coupling of l and s gives the total angular momentum number j for each nucleon and the total spin of a nucleus I is the sum of the j values. For even-A, I is an integer while for odd-A, I is a half-integer. This is because, as fermions, nucleons can only have a spin of $s = \pm 1/2$. As l is an integer, then j is a half-integer and thus the number of nucleons determines whether I is an integer or half-integer. The nucleus also has a parity quantum number π which is either even $(+)$ or odd $(-)$. The combined spin-parity of a nuclear state is indicated by I^{π} [14].

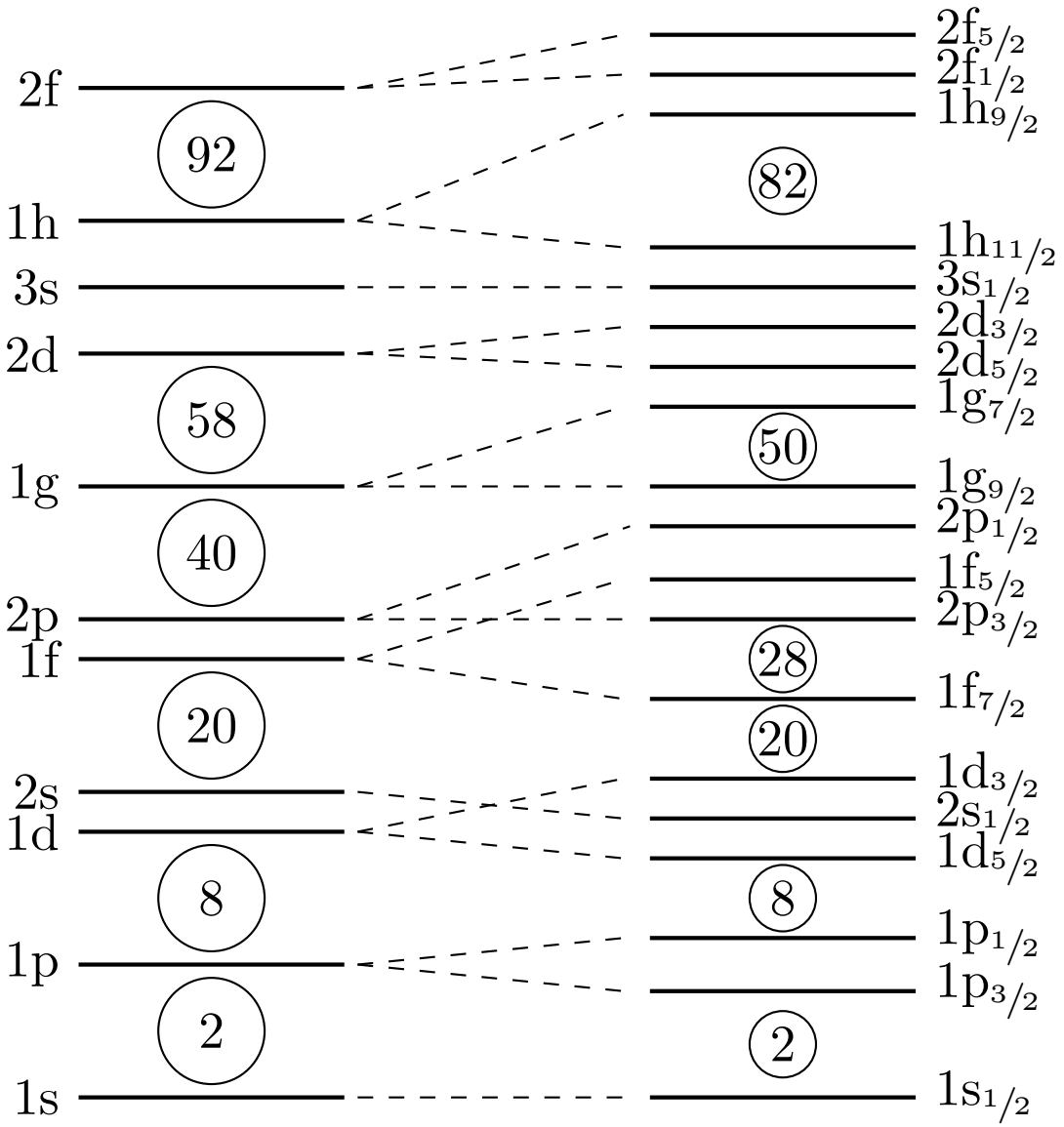

Figure 2.2: The single-particle orbits given by the Woods-Saxon potential (left) and corrected for the spin-orbit term (right). The protons and neutrons occupy separate sets of orbits. The circled numbers represent the magic numbers in both models, where nucleons are more tightly bound. Figure reproduced from Ref. [14].

Nucleon Configuration

The nucleons fill the orbits in by the shell model starting with the lowest-energy orbits and progressively filling higher-energy orbits. The orbits in the shell model are labelled in Fig. 2.2 by nl_j, where n is the index of the orbit, l is the orbital angular momentum and j is the total angular momentum. The ground-state configuration is formed by the nucleons filling orbits, starting at the lowest-energy orbits and filling upwards until every nucleon occupies an orbit. Nucleons tend to form pairs so that the net angular momentum between the two nucleons is zero. The spin-parity of the ground state is determined by the remaining unpaired nucleons. Nuclear excitations form when nucleons gain additional energy to move to higher-energy orbits or, equivalently, nucleon holes move to lower-energy orbits [14].

2.1.2 Nuclear Excited States

The nuclear shell model describes a number of states that the nucleus can occupy where each state has a discrete energy, spin and parity. The lowest-energy state is its ground state, while states of higher energy are its excited states. Excited states also have a lifetime which represents how long the nucleus occupies the state before transitioning to another state. The nucleus moves to excited states via excitations when it gains energy and decays to the ground state by emitting energy in a variety of forms. The excited states are connected by transitions, which represent the allowed excitation and decay paths. Research into nuclear structure is performed by measuring the properties of excited states through the transitions and interpreting what the results describe about the structure of the nucleus.

Level Scheme

The states and transitions of a nucleus are often presented in the form of a level scheme. The ground state is placed at the bottom of the level scheme and the excited states are placed in ascending energy order above it. The energy and the spin-parity of an excited state are listed next to the state if they are known. The level scheme also includes the known decay transitions and transition energies. An example level scheme is given in

Fig. 2.3.

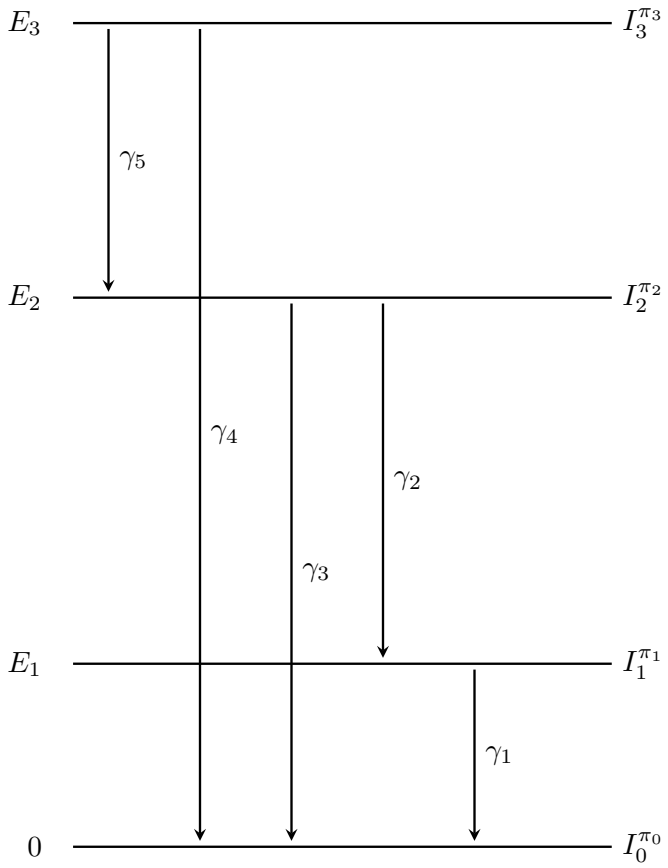

Figure 2.3: An example level scheme with three excited states and five transitions. The energy of the states are on the left and the spin-parities are on the right. The transitions are marked by arrows with the transition energy to the right of the arrow.

Single-Particle Excitations

In the shell model, nuclei near closed shells can be excited by the movement of a single nucleon to a higher-energy orbit. Nuclei with magic numbers of protons and neutrons are difficult to excite due to the large energy gap across a closed shell. Furthermore, the magic numbers are even so all of the nucleons will be in pairs. A paired nucleon requires additional energy to break the pairing in order to excite. Unpaired nucleons outside the closed shell are significantly easier to excite as they do not have to cross a shell gap or break a pairing to reach a higher-energy orbit. Therefore, the excitation of nuclei near closed shells occurs via the individual motion of the unpaired nucleons outside the closed shell. For example, both ^{121}Sb has 70 neutrons and a filled $Z = 50$ shell but also has an additional, unpaired proton outside the $Z = 50$ shell. The energy required to excite the

proton is significantly lower than excitations of the other nucleons. As a result, the low-energy excitations of ^{121}Sb are dominated by the single-particle excitation of the unpaired proton.

2.1.3 Collective Excitations

While single-particle excitations dominate near closed shells, nuclei in the regions away from shell closures exhibit 'collective' excitations as the number of nucleons outside the closed shell increases. Collective excitations comprise of the motion of many nucleons, with the two primary modes of excitation being vibrations on the surface of the nucleus and rotations of a deformed nuclear shape [14].

Nuclear Vibrations

A model of describing nuclear vibrations is the Liquid Drop Model, which compares the nucleons to molecules in a droplet of liquid. The resonance frequency of the vibration of a droplet is determined by the internal forces between the molecules and the droplet returns to its equilibrium shape due to forces associated with surface tension. Similarly, the shape and vibration of the nucleus is governed by a generalised force describing the complex interactions between nucleons. Due to the nucleon interactions, nuclei near shell closures have spherical shapes, while nuclei away from shell closures are deformed and have nonspherical shapes. [18].

In the Liquid Drop Model, the shape of a nucleus is determined by the motion of its nucleons and vibrational excitations are expressed by deformations in the nuclear shape. The deformation during a vibrational excitation can take on a range of shapes depending on the mode of the vibration. The larger vibrational modes are expressed by more complex deformation shapes, as depicted in Fig. 2.4. At time t, the radius of a point on the surface of a vibrating nucleus $R(t)$ at spherical coordinates (θ, ϕ) can be expressed as [14]

$$R(t) = R_{\text{av}} + \sum_{\lambda \geq 1} \sum_{\mu=-\lambda}^{+\lambda} a_{\lambda\mu}(t) Y_{\lambda\mu}(\theta, \phi), \tag{2.4}$$

where R_{av} is the average radius of the nucleus, λ is the vibrational mode number, $Y_{\lambda\mu}(\theta, \phi)$ are the spherical harmonics and $a_{\lambda\mu}(t)$ are the spherical harmonic amplitudes.

The energies of vibrational excitations are quantised as quasi-particles called phonons, where each phonon represents a vibrational mode. Excited states are formed by phonons coupling together and the energy and spin-parity of the state represent the phonons that give rise to the state. The lowest-energy vibrational states are given by a single phonon, while higher-energy states are given by multiple phonons. For example, suppose a nucleus begins in a 0^+ state. A single quadrupole phonon excites the nucleus to a 2^+ state, as it carries two units of angular momentum and even parity, while a single octupole phonon excites the nucleus to a 3^- state, as it carries three units of angular momentum and odd parity. Two coupled quadrupole phonons can excite the nucleus to a 2^+ or 4^+ state [14].

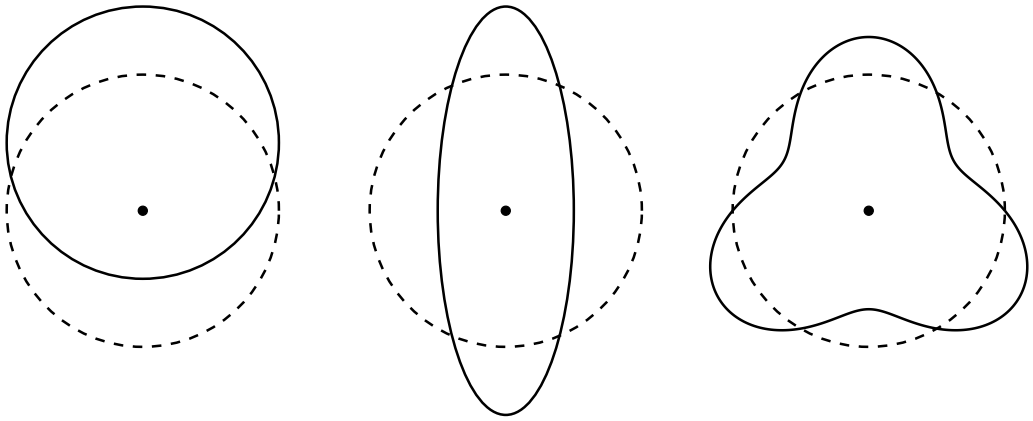

$\lambda = 1$ (Dipole) $\lambda = 2$ (Quadrupole) $\lambda = 3$ (Octupole)

Figure 2.4: Vibrational modes of a spherical nucleus. The dashed line represents the equilibrium shape and the solid line represents the vibrational deformation. Figure reproduced from Ref. [14] by Jack Woodside and used with permission.

Nuclear Rotations

Nuclei distant from closed shells have highly-deformed shapes and the deformations are expressed by the nucleus rotating around its axis of symmetry. Rotational excitations are common in nuclei in the mass number ranges of $150 < A < 190$ and $A > 220$.

The shape of a nucleus undergoing rotational excitation can be expressed by [14]

$$R(\theta, \phi) = R_{\text{av}} \left[1 + \beta Y_{20}(\theta, \phi)\right], \tag{2.5}$$

where β is the deformation parameter, given as

$$\beta = \frac{4}{3}\sqrt{\frac{\pi}{5}}\frac{\Delta R}{R_{\text{av}}} \tag{2.6}$$

where ΔR is the difference in length between the semimajor and semiminor axes of the nucleus. Nuclei with $\beta > 0$ have a prolate deformation, as depicted in Fig. 2.5, while nuclei with $\beta < 0$ have an oblate deformation. The magnitude of β determines the extent of the deformation.

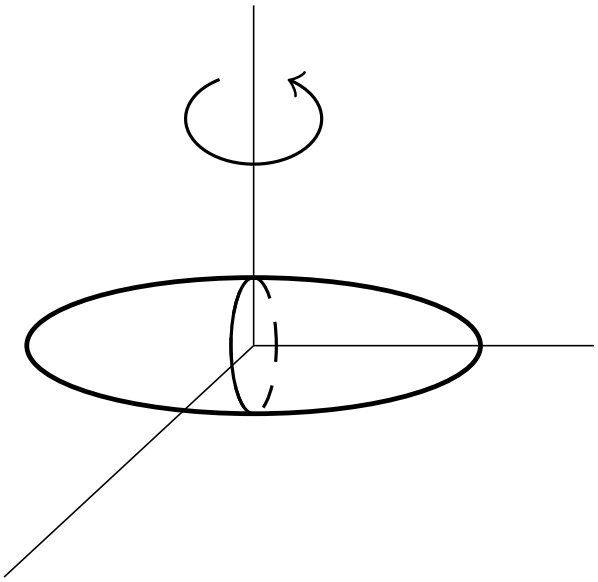

Figure 2.5: A prolate-deformed nucleus. As it has a deformed shape, it is able to be excited via rotations. Figure reproduced from Ref. [14].

The deformation of the nucleus is related to its intrinsic quadropole moment Q_0 by the expression [14]

$$Q_0 = \frac{3}{\sqrt{5\pi}} R_{\text{av}} Z\beta(1 + 0.16\beta). \tag{2.7}$$

The relationship between the quadrupole moment Q and Q_0 depends on the angular momentum of the nucleus.

The magnitude of the rotation is quantised to the moment of inertia of the nucleus. Therefore, the energies of the rotational excited states depend on the moment of inertia and the angular momentum of the nucleus. The energy of the rotating nucleus is given by

$$E = \frac{\hbar^2}{2\mathfrak{I}} I(I+1), \tag{2.8}$$

where $\mathfrak{I}$ is the moment of inertia and I is the nuclear angular momentum [14].

2.2 γ Decay

Nuclei release energy when they transition to a lower-energy state to maintain conservation of energy. One form of energy emission is a γ ray, a photon in the energy range from 10s of keV to around 10 MeV. The decay also has to maintain conservation of spin and parity, so the emitted γ ray has an associated spin-parity dependence on the states connected by the decay transition. Measuring the energies and timings of γ rays emitted during nuclear decay can be used to study nuclear structure [14].

Internal Conversion

Another mechanism for a nucleus to release energy when decaying is through internal conversion. The wavefunction of an electron in the atomic orbitals can interact with the nucleus. When the nucleus de-excites, the energy is transferred to the electron instead of being emitted as a photon. If the transition energy is greater than the binding energy of the electron, the electron is ejected from the atom. When internal conversion occurs, electrons move from higher-energy orbits to fill the gaps in lower-energy orbits. During this movement, the electrons emit energy in the form of an x-ray. As elements have unique configurations of electrons, the emitted x-rays are characteristic of the Z-number of the atom. [14, 19].

2.2.1 Transition Multipolarity

The spin and parity carried by a γ ray emitted by a de-exciting nucleus is represented by its multipolarity. In classical electromagnetism, the charge distributions of electric and magnetic fields are expressed as a sum of multipole moments. Each multipole moment produces a characteristic radiation field, allowing for the contributions of different multipoles to be measured [14]. Multipolarity can be considered in the quantum regime where the multipole moments are replaced by multipole operators. The multipole operator is a quantum mechanical operator that changes the nucleus from the initial state ψ_i to the

final state ψ_f, while producing a photon with the required energy and multipolarity. The multipole operator is represented by $m(\sigma L)$ where σ is either E for electric or M for magnetic and L is the multipole order. The reduced matrix element of the multipole operator of a transition from ψ_i to ψ_f is given by Ref. [20] as

$$m_{fi}(\sigma L) = \langle \psi_f || m(\sigma L) || \psi_i \rangle. \tag{2.9}$$

The reduced matrix element $m_{fi}(\sigma L)$ determines the decay probability of the transition. Typically, the dominant multipole is the lowest-order multipole that conserves angular momentum for the transition and the parity is determined by whether the transition is electric or magnetic. However, there are mixed transitions which have notable contributions from more than one multipole. For example, a 507-keV transition of ^{121}Sb has a multipolarity of $M1 + E2$ as it has significant contributions from both its $M1$ and $E2$ multipoles.

Multipolarity Selection Rules

The quantity of angular momentum carried by an emitted photon is equal to the multipole order L. As angular momentum has to be conserved, the allowed multipole contributions are determined by the difference in spin between the initial state I_i and final state I_f [14]. This restricts the possible values of L to

$$|I_f - I_i| \leq L \leq |I_f + I_i|. \tag{2.10}$$

For example, if $I_f = \frac{9}{2}$ and $I_i = \frac{5}{2}$, then the multipoles that contribute to the transition are between $L = 2$ and $L = 7$.

There are also parity selection rules which determine whether the multipole is electric or magnetic based on the multipole order and parity of the transition. The parity selection rules state

$$\begin{aligned} \pi(ML) &= (-1)^{L+1}, \\ \pi(EL) &= (-1)^{L}. \end{aligned} \tag{2.11}$$

For example, if $L = 2$ and the transition is from a $9/2^+$ state to a $5/2^+$ state, then by Eq. 2.11 the transition multipole is electric.

2.2.2 Transition Probabilities

As discussed in Section 2.1.1, nucleons in the shell model prefer to pair up, which leaves a single, unpaired nucleon in odd-A nuclei [14]. As paired nucleons have a net angular momentum of zero, the properties of the nucleus can be assigned based on the properties of the unpaired nucleon. This allows for a single-particle model for transitions in odd-A nuclei to be constructed, with the model assuming the remaining nucleons are paired up and do not contribute to the multipole moments [21].

Within the single-particle model, the reduced transition probability is given in Ref. [21] as

$$\begin{aligned} B(\sigma L; I_i \to I_f) &= \frac{1}{2I_i + 1} \langle \psi_f || m(\sigma L) || \psi_i \rangle^2, \\ &= \frac{m_{fi}(\sigma L)^2}{2I_i + 1}, \end{aligned} \tag{2.12}$$

where I_i and I_f are the nuclear spins of the initial and final states respectively. The single-particle model also allows for an approximation known as the 'Weisskopf estimate' to be determined. The Weisskopf estimate is the reduced transition probability of a purely single-particle interaction for a specific multipole. For example, the Weisskopf estimate of a $B(E2)$ value for a nucleus of mass number A in units of $e^2\mathrm{b}^2$ is given by

$$B_{\mathrm{W.u.}}(E2) = 5.94 \times 10^{-6} A^{\frac{4}{3}}. \tag{2.13}$$

Dividing the result of Eq. 2.12 by the corresponding Weisskopf estimate gives the reduced transition probability in Weisskopf units (W.u.), which approximate how many nucleons were involved in the transition. Transition probabilities in W.u. are close to one for single-particle-like excitations and larger for collective excitations.

Nuclear models are capable of making predictions of transition probabilities but the accuracy of the predictions are limited by the complexity of the model. Experiments are needed to verify the results of the model. A way of evaluating a model is by determining

the transition probabilities through experimentation and comparing the values to predictions. I have calculated the transition probabilities experimentally by measuring the γ-ray yields of ^{121}Sb and using the yields to calculate the reduced matrix elements.

Electric Quadrupole Moments

In Eq. 2.12, the off-diagonal matrix elements of the multipole operator correspond to the transitions between states while the diagonal elements correspond to the static multipole moments. Due to the reorientation effect, the static electric quadrupole moment can significantly contribute to the cross-section in Coulomb excitation. The electric quadrupole moment for a nucleus with spin I is related to the reduced matrix element by the equation from Ref. [22]

$$Q(I) = \sqrt{\frac{16\pi I(2I-1)}{5(2I+1)(I+1)(2I+3)}}\langle I||m(E2)||I\rangle. \tag{2.14}$$

2.3 Isomers

Most excited states have lifetimes in the order of femtoseconds; however, there are excited states with significantly longer lifetimes. These long-lived states are known as isomers and have lifetimes that can range from nanoseconds to 10^{15} years [11]. Isomers form when all of the decay transitions from an excited state are inhibited. In the absence of excitation energy, nuclei in excited states can only transition to a lower-energy state. If the decay pathways to the lower-energy states are inhibited, the nucleus is then trapped as it is restricted from transitioning to another state.

2.3.1 Types of Isomers

Transitions between excited states can be inhibited by a number of factors and isomers are classified based on the main factor that hinders the decay transitions.

A common type of isomer is the spin-trap isomer, where the difference in angular momentum between excited states inhibits the decay transitions. Transitions must have a multipolarity, L, equal to or greater than the difference in angular momentum between the connected states. Transitions with a multipolarity of $L = 1$ or $L = 2$ are very common,

however, increasing the multipolarity of a transition significantly decreases the transition probability. For every step of increase in multipole order, the transition probability decreases by a factor of approximately 10^{-5} [14]. If the angular momentum difference between states is large enough, then the transition is inhibited as the required L has a reduced transition probability. For example, an isomer of ^{180}Ta forms because the multipolarity of a transition to the ground state is $L = 8$. This reduces the transition probability by a factor of approximately 10^{-35} compared to an $L = 1$ transition [11, 14].

A variant of the spin-trap isomer is the K-trap isomer. K is a quantum number representing the projection of nuclear spin I onto the symmetry axis of the nucleus [23]. This is particularly relevant for nuclei with prolate deformations, as they have longer symmetry axes compared to spherical nuclei. L must be greater than the change in K-number so that the transition conserves angular momentum. Therefore, the isomer forms if the decay transitions have a large change in K [23]. An example of a K-trap isomer is a 1.1 MeV excited state of ^{178}Hf with $K = 8$. The most probable decay transition is an excited state with $K = 0$. As L is less than the change in K, the transition is hindered, forming an isomer [11].

A third type of isomer is the shape isomer. Transitions are strongest between states that have a strong overlap of their radial wavefunctions. As mentioned in Section 2.1.3, many nuclei have nonspherical shapes due to deformations on the nuclear surface. The deformations in the shape of a nucleus can decrease the overlap between the excited state wavefunctions, reducing the transition probability. Shape isomers occur when the deformations have decreased the wavefunction overlap to the point that the decay transitions are inhibited, trapping the nucleus in the isomer [24].

A version of the shape isomer is the fission isomer which occurs in nuclei that are super deformed. In this instance, the excited state wavefunction overlap has been reduced by such an extent that the nucleus decays from the isomer via a nuclear fission reaction rather than through γ decay. This inhibits the transition as the nucleus has to gain energy to overcome the fission energy barrier and transition out of the isomer. Fission isomers have been mainly observed in nuclei in the actinide region of the periodic table [25, 26].

2.4 Structure of ^{121}Sb

The evolution of single-particle structure is driven by the non-central, tensor component of the nucleon-nucleon interaction [27]. Its effects on nucleons in a nucleus can be described through the collision of two nuclei in different j-states. The high relative angular momentum of the j-states means that there is a limited distribution of the spatial wavefunction that is orientated parallel to the spin projection. This is due to Heisenberg's Uncertainty Principle which limits the range of position Δx relative to linear momentum Δp so that $\Delta x \cdot \Delta p \sim \hbar/2$ [14]. The orientation parallel to the spin projection is prolate, therefore prolate deformations are favoured by the tensor interaction between the nuclei. Thus prolate nucleon distributions have a greater degree of radial overlap between orbits than oblate distributions [28].

The single-particle evolution picture can be applied to the structure of isotopes of antimony. As described in Section 2.1.1, it is expected that the orbits in the shell model are filled progressively by nucleons. However, the five neutron orbits located in the shell between $N = 50$ and $N = 82$ are very close in energy and pairing correlations between nucleons lead to similar energy differences between each orbit. This results in the orbits appearing to be filled simultaneously instead of progressively. The simultaneous filling of the $\nu h_{11/2}$ orbit leads to an attractive interaction with the $\pi g_{7/2}$ orbit due to the non-central tensor component. Increasing the number of neutrons in the $\nu h_{11/2}$ orbit causes the $\pi g_{7/2}$ orbit to be more tightly bound, decreasing its energy [28]. This can be observed in the evolution of the ground state of antimony nuclei.

Antimony nuclei with odd mass numbers have one unpaired proton outside the $Z = 50$ shell, which represents the key properties of the ground state such as spin-parity. For antimony nuclei with odd mass numbers below $A = 121$, the unpaired proton occupies the $\pi d_{5/2}$ orbit, so the spin-parity of the ground state is $5/2^+$. As pairs of neutrons are added to the $\nu h_{11/2}$ orbit, the energy of the $\pi g_{7/2}$ orbit decreases. At odd mass numbers $A = 123$ and higher, the $\pi g_{7/2}$ orbit has less energy than the $\pi d_{5/2}$ orbit. Therefore, the unpaired proton occupies the $\pi g_{7/2}$ orbit, switching the spin-parity of the ground state to $7/2^+$, as illustrated in Fig. 2.6.

As the heaviest isotope of antimony with a ground state spin-parity of $5/2^+$, the $\pi g_{7/2}$

and $\pi d_{5/2}$ orbits of ^{121}Sb are very close in energy. This results in the first excited state of ^{121}Sb being only 37 keV above the ground state. This is low compared to other nuclear excited states; the first excited states of the odd-A antimony nuclei in Fig. 2.6 are all an order of magnitude higher in energy. The 37-keV excited state is also an isomer with a mean lifetime of 4.99(4) ns [29]. The low-energy isomer is suitable for testing energy release mechanisms as it does not require a high interaction energy to populate.

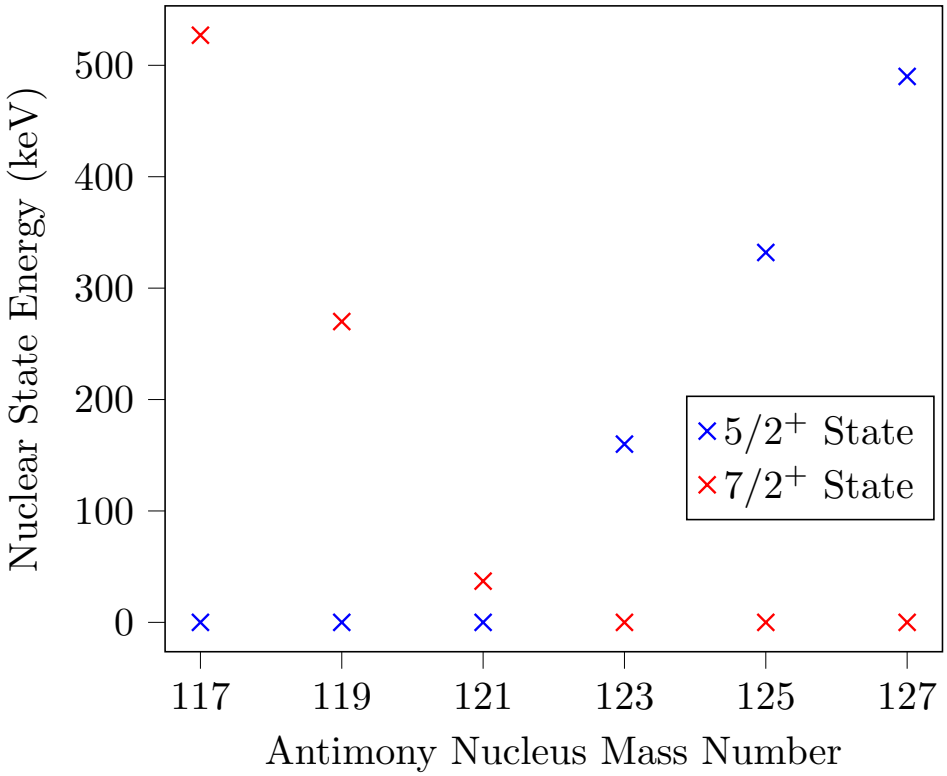

Figure 2.6: Energy and spin-parity of the ground state and first excited state for antimony nuclei as the mass number increases. Energy and spin-parity data obtained from Ref. [29–34].

2.5 Coulomb Excitation

5A technique that can be used to access excited states of a nucleus is Coulomb excitation. In Coulomb excitation, a beam of ions is used to bombard a target nucleus; the nuclei interact via the Coulomb force and undergo inelastic scattering demonstrated in Fig. 2.7. The energy of the beam is selected such that the Coulomb force contribution is maximised while the contribution of the nuclear strong force is minimised. An advan-

tage of Coulomb excitation is that the minimised strong force contribution means that nuclear interactions, such as fusion, are highly unlikely to occur. Thus the target nucleus is excited without experiencing changes to its nuclear structure. In the context of isomer energy-storage, this allows the nuclei to be excited into the isomer as the structure of the nucleus has not changed, extending the lifespan of the energy-storage device. Due to the energy scales of the electromagnetic interaction, Coulomb excitation favours populating low-energy excited states (excited states below 1 MeV) through population transitions with $E2$ multipolarities [35, 36]. This provides another advantage as the transition probabilities can be calculated from the $E2$ matrix elements. These factors potentially make Coulomb excitation an effective mechanism for exciting nuclei out of low-energy isomers. To determine whether the assumptions made in the semi-classical theory of Coulomb excitation are valid at low-energy, I performed a γ-ray spectroscopy on a Coulomb-excited ^{121}Sb target and compare the transition probabilities to values determined from other experiments.

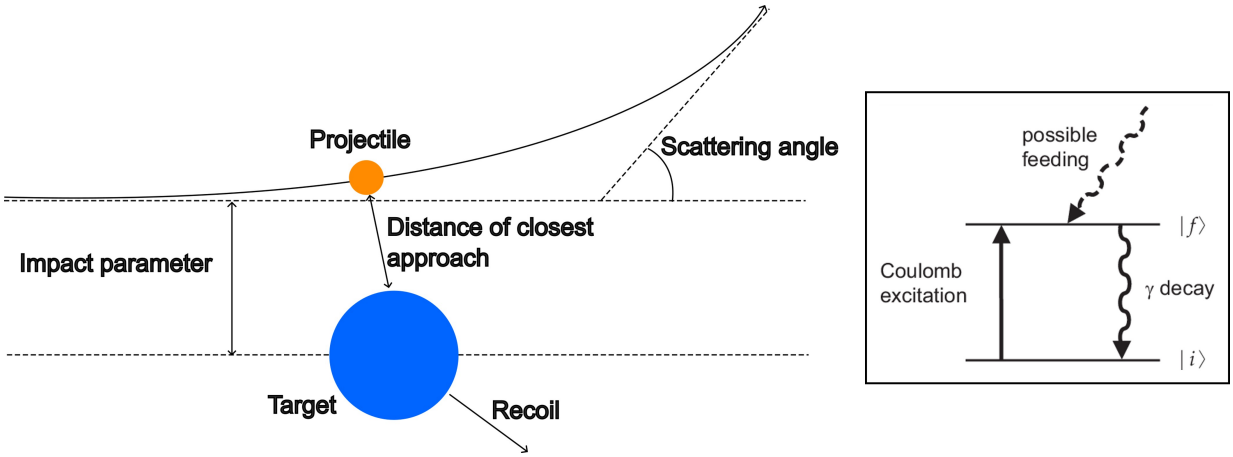

Figure 2.7: Schematic diagram of a Coulomb-excitation interaction (left). Diagram of excited-state population and decay via Coulomb excitation (right). Figure on right from Ref. [37]

2.5.1 Experimental Considerations

The theoretical models of Coulomb excitation assume a purely Coulomb interaction but a nuclear-strong force component will always be present in any interaction between two nuclei. Strong force interactions act at a shorter range than Coulomb interactions so the strong force contribution can be minimised by selecting a beam energy leading to

an interaction distance greater than the strong force distance. To approximate a pure Coulomb interaction experimentally, the energy of the interaction must be selected such that the distance of closest approach between the nuclei is always greater than 5 fm [35]. The 'safe' energy in MeV is given by the equation in Ref. [38] as

$$E_{\text{safe}} = 1.44 \frac{A_{\text{beam}} + A_{\text{target}}}{A_{\text{target}}} \frac{Z_{\text{beam}} Z_{\text{target}}}{1.25(A_{\text{beam}}^{\frac{1}{3}} + A_{\text{target}}^{\frac{1}{3}}) + 5}. \tag{2.15}$$

When selecting a beam species for Coulomb excitation, the charge and excited state configuration of the species have to be considered. As indicated in Eq. 2.15, the safe energy is dependent on the charge product of the beam and target nuclei. Therefore, selecting a beam nucleus with a high Z-number will allow for higher-energy beams, increasing the amount of excitation that occurs.

The nature of Coulomb excitation means that both the beam and target nuclei are excited during the interaction. If the beam excitations produce γ rays in the same energy range as the target, then the target γ-ray spectrum will be contaminated with γ rays emitted from the beam nuclei. This can be negated by selecting a beam nucleus with excited states above the energy range of states being investigated in the target [38]. Doubly-magic nuclei such as ^{16}O are often chosen for this reason.

2.6 γ-ray Spectroscopy

As described in Section 2.2, when a nucleus decays, it emits a γ ray with an energy equal to the energy difference between the excited states minus a small recoil contribution. As the excited states have discrete energies, the energy of the emitted γ ray is characteristic of the de-excitation transition [39]. Measuring the spectrum of γ rays emitted by a nucleus undergoing de-excitation can provide information on the excited states and structure of the nucleus.

2.6.1 Photon Interactions

The photons detected by a γ-ray detector can undergo different interactions, affecting the properties that are measured during the experiment.

A photoelectric interaction is where an electron in an atomic shell absorbs a photon and is ejected from the atom. The probability of the interaction is proportional to the Z-number of the atom and inversely proportional to the energy of the photon. Therefore, photoelectric interactions are more likely to occur in photons with energies below 100 keV [40].

Another photon interaction is Compton scattering, where a photon collides with a free electron. The collision results in some kinetic energy being transferred to the electron and the photon having a lower energy and altered trajectory. As the interaction occurs with a free electron, the interaction probability only depends on the energy of the photon. Compton scattering dominates interactions of photons in the 100-10^4 keV energy range [40].

A third type of photon interaction is pair production. When a photon interacts with the electric field of an atomic nucleus, it is possible for the photon energy to be converted into an electron-positron pair. This interaction requires photons with energies greater than 1.022 MeV, the combined rest mass energy of an electron and a positron, to maintain conservation of energy. Extra photon energy is converted into kinetic energy for the electron and positron [40].

2.6.2 γ-ray Detectors

To measure the γ rays emitted during the excitation, specialised detectors are required to record the energy and timing of the γ rays. There are multiple different types of γ-ray detector such as photometers and scintillation detectors [39]. As this experiment involves multiple γ rays in a relatively small energy range, high-purity germanium (HPGe) semiconductor detectors were used as these detectors have a high energy resolution. Semiconductors have regions where electrons are not free to travel without an additional source of energy, known as the bandgap. When a γ ray enters the detector, it provides energy for electrons to cross the bandgap. The movement of charges creates a pulse that is proportional to the energy of the γ ray. A preamplifier converts the charge pulse to a voltage pulse, which can be used to record the energy of the γ ray. Germanium is used in the detectors because it has a bandgap of 0.67 eV, the smallest bandgap of any semiconductor

[39]. The small bandgap gives HPGe detectors a level of precision to about 1 keV, however it also provides a source of noise. Due to the small bandgap in germanium, background thermal energy is capable of exciting electrons across the bandgap, introducing noise into the γ-ray spectrum. Thermal electron noise in HPGe detectors is reduced by keeping the detectors at a low temperature [39, 41].

2.6.3 Compton Suppression

While HPGe detectors have a high energy resolution, only a fraction of the γ rays deposit their full energy into the crystal within the detector, leading to low detector efficiencies. For example, tests at Argonne National Laboratory in the USA discovered that a 1-MeV γ ray only deposited its full energy on a 49 cm^2 germanium crystal 25% of the time [42]. One of the causes of the low efficiency were Compton scattering events described in Section 2.6.1. The Compton events meant the γ rays were being measured at a lower energy than when they were emitted from the target, thus decreasing the number of counts at the expected transition energies. It also broadened the transition peaks on the energy spectra as the range of energies corresponding to a transition increased. The effect of Compton scattering is reduced by using Compton-suppression shields, placed around the γ-ray detector. If two γ rays are detected in coincidence between the γ-ray detector and Compton suppressor, the γ ray is recorded as a Compton event and can be removed from the spectrum during data analysis. My experiment utilised bismuth germanate (BGO) Compton-suppression shields to reduce the effect of Compton events on the experiment.

2.6.4 Particle Detection

The γ-ray detectors were supplemented by particle detectors to record the number of beam particles that scattered off the target. The particle detectors allow for particle-γ coincidences to be taken, which determine the type of interaction and are used to reduce the background in the energy spectra. Particle detectors also give the kinematics needed for Doppler corrections and the particle scattering angles are used in Coulomb-excitation analysis, both of which are discussed in detail in Chapter 4. The particle detectors used in the experiment were silicon photodiodes, which operate on similar principles to the

HPGe γ-ray detectors. When a particle enters the photodiode, it excites electrons over the semicondutor bandgap, creating a charge pulse that records the energy of the particle [43].

2.6.5 Data Acquisition

The output signals from the γ-ray detectors, Compton shields and particle detectors are input into a XIA Pixie-16 digitiser [44]. The digitiser is triggered on a range of pulse conditions. For example, the trigger for the Compton suppressors are connected to when the HPGe detectors register an event. The digitiser uses the properties of the voltage pulse to determine the energy and timing of an event for each detector. The raw data is converted into events with the signal energies, timing and detector identifier. The timings are also used to measure events in coincidence, where two detectors measure signals that are considered a single event. The time window for a event construction used in this experiment was 3 µs.

2.7 Experiment Plan

The plan for my experiment was to Coulomb excite an ^{121}Sb target with an ^{16}O beam in order to exam the behaviour of Coulomb excitation at low energies. As mentioned in Section 2.5.1, a suitable beam for Coulomb excitation has transitions that do not overlap with the target. Oxygen-16 has $Z = 8$ and $N = 8$, meaning it is a 'doubly-magic' nucleus as all of its nucleons are in closed shells. As a result, its first excited state is 6 MeV above the ground state [45]. This is above the energy range of the ^{121}Sb states I am investigating, which are all less than 1.5 MeV above the ground state. Therefore, there was no possibility of the γ-ray spectrum being contaminated by ^{16}O transitions.

To prepare for which transitions of ^{121}Sb would be expected on the energy spectrum, **Gosia** simulations were performed. **Gosia** is a software suite designed for the analysis of Coulomb-excitation data that will be discussed in more detail in Chapter 4 [38]. Antimony-121 data from Ref. [29] was input into **Gosia** to generate Coulomb excitation yields. This helped improve my understanding of how to use **Gosia** and gave an indication of the transitions that I should have expected to see in the experimental spectra.

I familiarised myself with the equipment used in the experiment by participating in setup work in the laboratory. The setup involved installing pre-amplifiers that would convert detector pulses into voltage pulses for the digitiser. I also regularly filled the γ-ray detectors with liquid nitrogen to reduce the noise produced by thermal electrons and learnt how to place the target chamber under vacuum so it could be used for experiments.

Another part of my preparation was learning how to process the experimental data for analysis. The data recorded on the digitiser had to undergo post-processing to calculate the γ-ray yields from the raw data. This included calibrating the detectors, aligning the particle and γ-ray spectra and correcting for factors such as detection efficiency. I performed a simulation of this procedure by processing ^{56}Fe Coulomb-excitation data from a previous experiment. The analysis process will be discussed in more detail in Chapter 4.

Chapter 3

Experiments

This thesis presents work from a beamtime allocation at the Heavy Ion Accelerator Facility (HIAF) at ANU. The experiment aimed to Coulomb-excite ^{121}Sb using an accelerated beam of ^{16}O ions. The data collected would be used to determine transition probabilities that would then be compared to values in the literature.

3.1 14UD Accelerator

The ^{16}O beam was delivered to the ^{121}Sb target using the 14UD tandem accelerator at HIAF [46]. The 14UD has the ability to accelerate ions ranging from hydrogen to plutonium to velocities up to approximately 0.1c. The accelerator delivers an ion beam in a multi-step process, beginning with a sample containing atoms of the beam species being inserted into a cathode and sputtered by caesium. The sputter process produces ions in a $q = -1$ charge state, which are then pre-accelerated to an energy of 150 keV before injection into the accelerator. The ions pass through a dipole magnet, which produces a magnetic field that only directs ions with the charge-to-mass ratio of the selected beam species into the accelerator. This removes contaminant ions generated during sputtering by impurities in the sample. The accelerator operates at an adjustable terminal voltage of up to +15 MV, which is generated by three pelletron chains. The negative ions are attracted to the positive terminal, accelerating the ions to an energy of eV_t, where V_t is the terminal voltage and e is the charge of an electron. At the terminal, a thin carbon foil strips electrons from the ions, changing the ions to a new charge state, $+q$. The now positive ions are then repelled by the terminal towards the bottom of the accelerator with additional energy of qV_t. At the bottom of the accelerator is an analysing magnet, which

directs beam ions in the desired charge state into the target area. Additional magnets are used to direct the beam down the beamline used for the experiment [46]. A diagram of the accelerator facility is presented in Fig. 3.1.

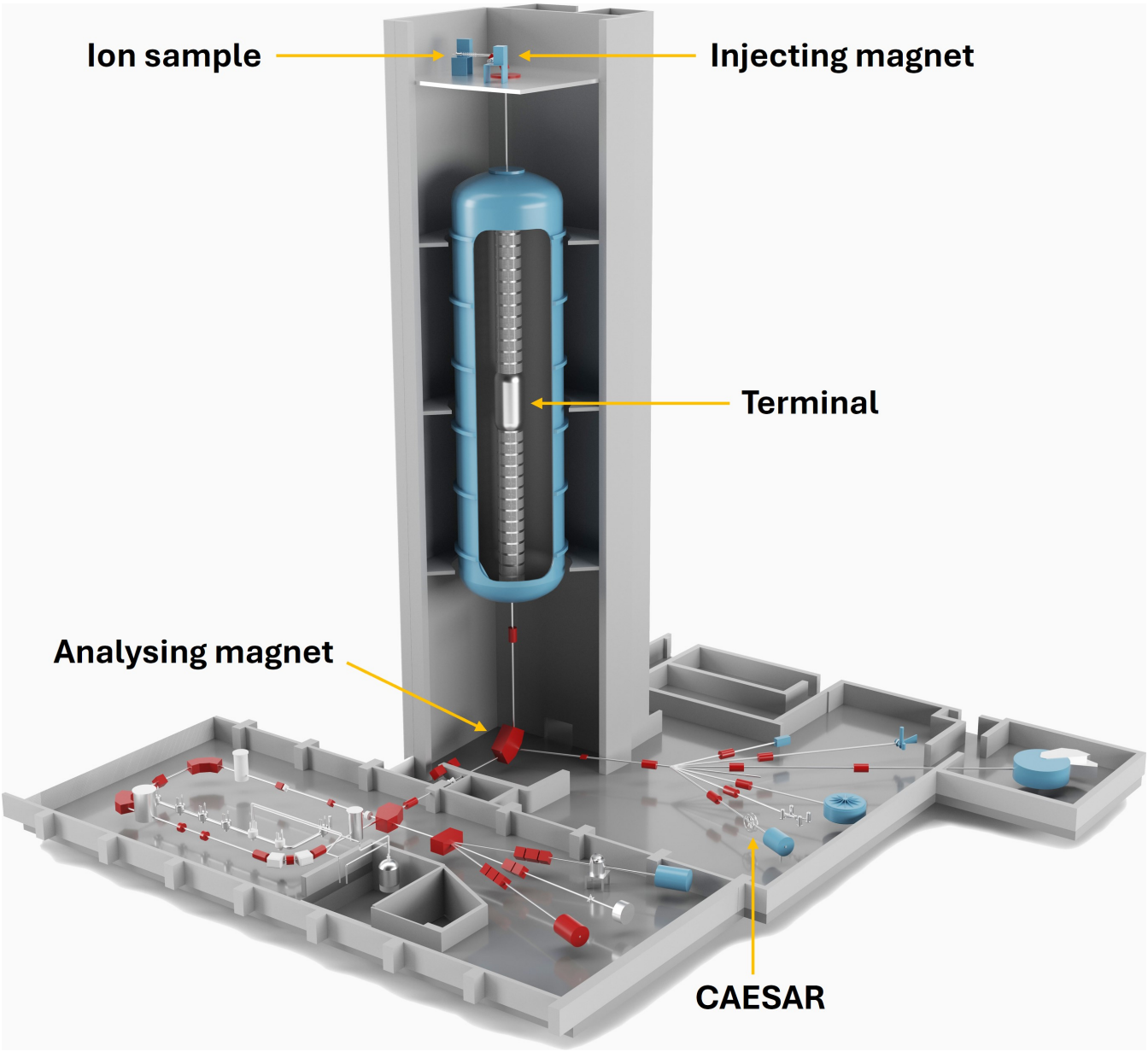

Figure 3.1: 3D render of the 14UD accelerator facility. Created by HIAF technical staff.

3.2 CAESAR

Gamma-ray spectroscopy of the excited nuclei was performed using the Compton-Suppressed Array (CAESAR) at HIAF. CAESAR consists of a target chamber surrounded

by nine BGO Compton suppressors that house the HPGe γ-ray detectors, as seen in Fig. 3.2a. The BGOs are set to trigger if a signal is detected in coincidence with the corresponding HPGe detector. The coincidence indicates that a γ ray has not deposited all of its energy into the HPGe, marking it as a Compton event. This allows for Compton events to be suppressed during the data analysis, resulting in cleaner spectra [41]. The HPGe detectors were placed at a range of angles, listed in Table 3.1, to provide wide coverage of the target chamber. They required regular cooling using liquid nitrogen to reduce noise generated by thermal electron excitations. The target chamber contains the target which was mounted on a movable target ladder surrounded by the particle detector array.

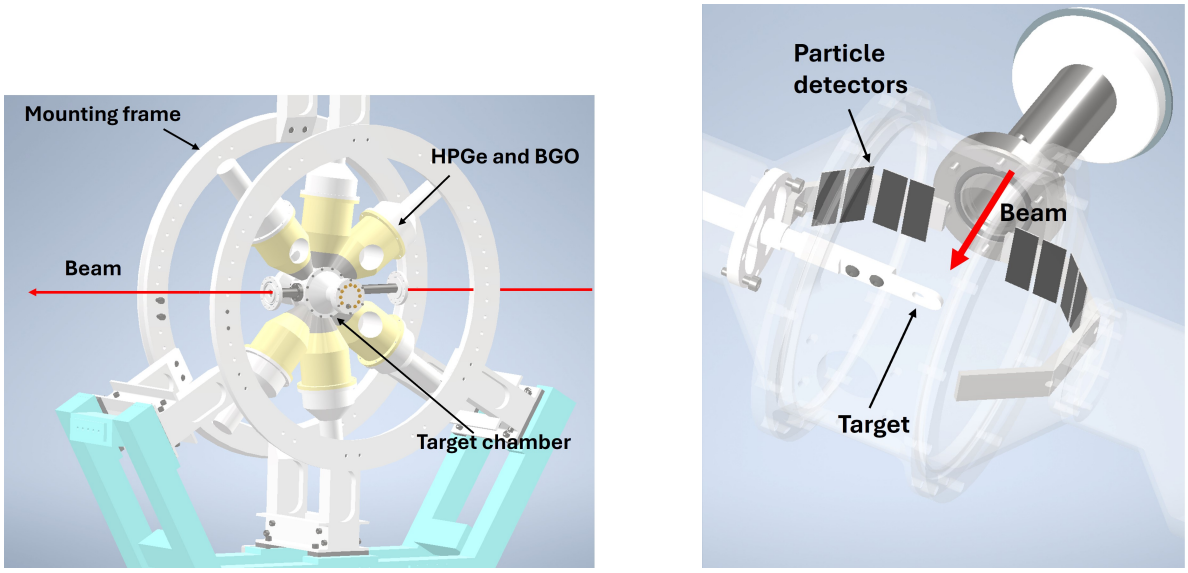

(a) (b)

Figure 3.2: (a) 3D render of CAESAR. The HPGe detectors are inserted into the holes on the side of the BGOs. The beam travels from right to left through the target chamber. Only six of the nine BGOs are visible in the render. (b) 3D render of the CAESAR target chamber with particle detectors installed. 3D renders created by Tom Tunningley and modified by Martha Reece.

The data were recorded by inputting the output signals of the photodiodes, HPGe detectors and BGO suppressors into the Pixie-16 digitiser. The digitiser then sorts the signals into time-ordered 'events' that contain properties of the signal and the detector that produced it. The digitiser is triggered on a range of pulse conditions. For example, the BGOs are only triggered in coincidence with an HPGe detector.

HPGe Detector	θ (degrees)	ϕ (degrees)
G1	144.5	90.0
G2	96.5	90.0
G3	48.0	90.0
G4	146.0	270.0
G5	98.0	270.0
G6	49.5	270.0
G7	131.6	168.2
G8	48.7	0.0
G9	52.6	171.9

Table 3.1: Angles of HPGe γ-ray detectors in CAESAR. Note that detector G1 was not used during the experiment. Furthermore, the data from detector G5 were not included in the final analysis as they were poor quality.

Photodiode	θ (degrees)	ϕ (degrees)
A	122.4	180.0
B	133.0	180.0
C	144.1	180.0
D	154.4	180.0
E	151.1	0.0
F	141.2	0.0
G	130.6	0.0
H	120.2	0.0

Table 3.2: Angles of the silicon photodiode particle detectors within the target chamber.

3.3 Particle Detector Array

The particle detector array consisted of eight rectangular silicon photodiodes with an area of $25.15 \times 9.25\,\mathrm{mm}^2$. Like the HPGe detectors, the photodiodes were positioned at a range of angles, listed in Table 3.2, to detect scattered particles with a range of trajectories. The photodiodes were wrapped in 6 µm of aluminised mylar which prevented visible light

from reaching the photodiodes. The particle detector array was arranged symmetrically about the beam axis at backwards angles on the horizontal axis, as depicted in Fig. 3.2b.

3.4 Experiment Conditions

The HPGe detectors were installed into the BGOs in CAESAR and the photodiode detectors were placed in the target chamber. During a prior experiment, HPGe detector G1 stopped working, so it was present in the set-up but was not used to record any data.

The Coulomb excitation of ^{121}Sb was performed using a 44 MeV ^{16}O beam. Oxygen-16 was selected for the reasons discussed in Section 2.7; the configuration of excited states meant it was highly unlikely for ^{16}O transitions to contaminate the ^{121}Sb γ-ray spectra. The beam energy of 44 MeV was below the safe energy of 46.4 MeV for a Coulomb excitation experiment of an ^{16}O beam on an ^{121}Sb target, calculated from Eq. 2.15.

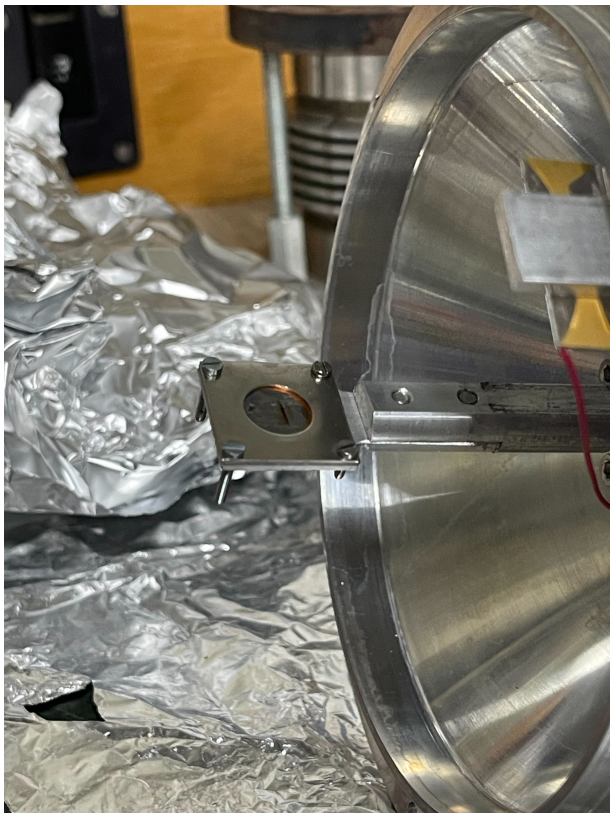

Figure 3.3: The ^{121}Sb target in the target chamber following the completion of the experiment.

The target holder was set to a height that placed the target at the geometric centre

of the target chamber, as demonstrated by Fig. 3.3. The original ^{121}Sb target was manufactured at Argonne National Laboratory in the USA, however it was found to be broken when being prepared for the experiment. This required the use of a different ^{121}Sb target manufactured at ANU by Professor Andrew Stuchbery. The new target had a thickness of $0.49\,\mathrm{mg\,cm^{-2}}$ and was held in a target holder with a 15-µm copper backing to prevent breakages. Antimony has two stable isotopes, ^{121}Sb and ^{123}Sb, which are both present in naturally-occurring sources of antimony. Therefore, the ^{121}Sb target was enriched to remove ^{123}Sb impurities. The target used was enriched to approximately 99.56% ^{121}Sb and 0.44% ^{123}Sb.

Over a period of five days, the target was bombarded by an ^{16}O beam, exciting the ^{121}Sb nuclei and producing γ rays. The γ-ray timings, counts and energies were measured by the various detectors in CAESAR and recorded on the digitiser. Following the completion of the experiment with the ^{121}Sb target, radioactive sources of ^{152}Eu, ^{133}Ba and ^{207}Bi were placed separately in the target chamber. The γ-ray spectra produced by the radioactive sources were used for calibrating CAESAR and calculating the HPGe detection efficiencies.

I contributed to the setup and operation of the experiment by helping to install the HPGe detectors and preamplifiers as well as venting the target chamber so it was under vacuum. I took shifts in the accelerator along with other members of the research group to manage the experiment. While on shift, I monitored the beam current and adjusted the apertures and magnets within the accelerator to ensure the beam was on target and at the right current level. I also monitored the data acquisition system to check for crashes and was responsible for alerting the technical staff if there was a significant problem that required their attention. In addition to my experiment, I was also involved in two other experiments using the accelerator throughout the year. The first was a test of angular correlations for ^{124}Te and the second was a lifetime measurement of ^{188}Pt. In both experiments, I volunteered for shifts in the accelerator. This further increased my experience in operating the accelerator during an experiment.

Chapter 4

Data Analysis

The data recorded by the digitiser had to be processed before it could be input into **Gosia**. This involved sorting the events, calibrating the HPGe detectors in energy and efficiency and placing gates around the spectra so that random particle-γ coincidences are removed. The different angles of the detectors also had to be accounted for by performing angular correlation measurements.

4.1 Sorting Raw Data

The first step in the analysis was sorting the raw data from the digitiser into energy spectra. The γ-ray spectra were viewed and analysed in ROOT, a program developed by CERN for analysing data from particle physics experiments [47]. However the output data from the Pixie was in the form of lists of time-ordered events. The data needed to be sorted into a file that could be viewed in ROOT. The sorting was performed using a code (**CaesarSort**) developed by the research group. **CaesarSort** takes the raw data from the digitiser and sorts the events into a file for the ROOT framework.

4.2 Calibrations

4.2.1 Energy Calibrations

The first step was to perform energy calibrations on the detectors using the calibration sources. The ^{152}Eu, ^{133}Ba and ^{207}Bi sources had transitions with well-known energies and relative intensities, so they were useful for energy calibrations. Additionally, the range of peak energies across the three calibration sources improved the detection efficiency

corrections. The efficiency of HPGe detectors varied with energy, so the efficiency correction was performed by fitting an efficiency curve to the calibration data. The excited states of ^{121}Sb being investigated had energies ranging from the order of 10 keV to 1 MeV. Therefore, a range of peak energies were needed to ensure the fit was accurate across the energy range. This was particularly important for the 37-keV transition, as the low-energy efficiency of HPGe detectors was difficult to determine. The peak energies of the three sources cover the necessary energy range and therefore are useful for performing efficiency calibrations.

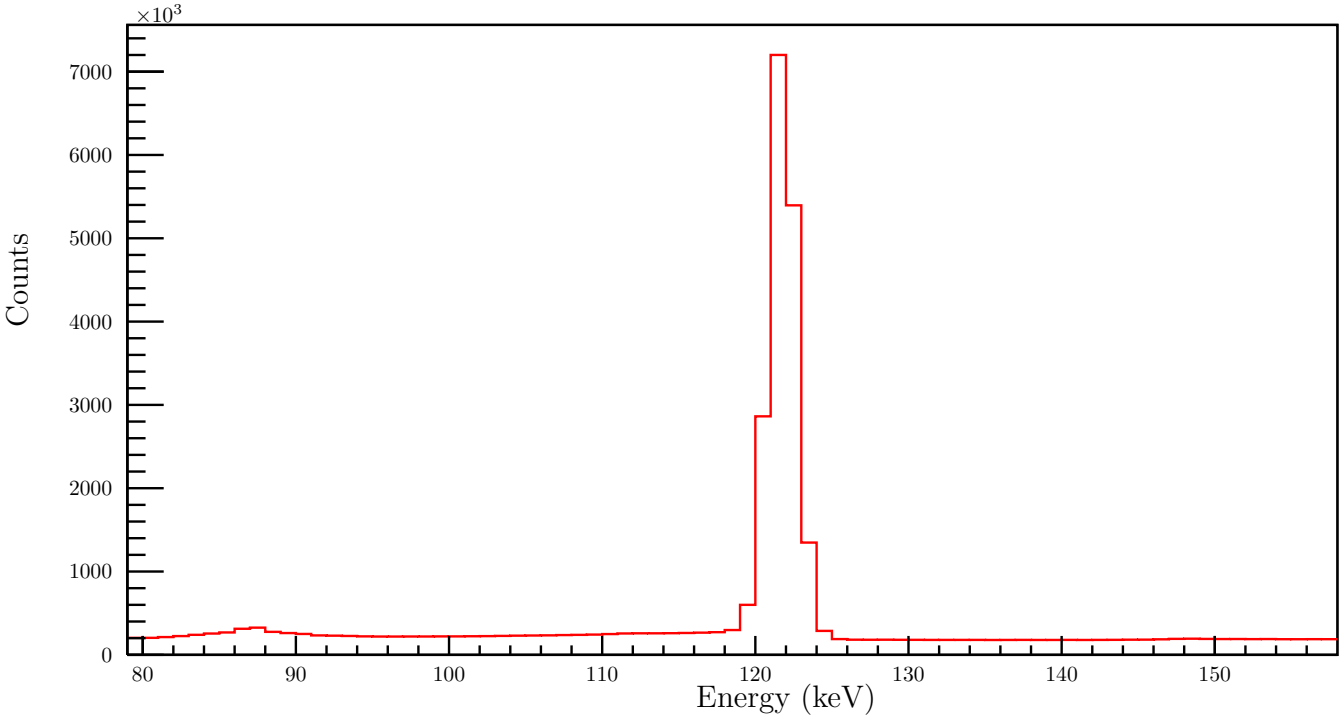

Figure 4.1: The 122-keV peak in the ^{152}Eu energy spectrum. A Gaussian fit was used to measure the centroid of the peak, which corresponds to the energy of the peak.

The ^{152}Eu source was used for the HPGe energy calibrations as it has the highest number of well-known transition energies and intensities of the three sources. The centroids of the peaks on the energy spectra were identified by fitting Gaussian functions despite the peaks not taking Gaussian shapes, as illustrated in Fig. 4.1. This was because the Gaussian function is able to accurately identify the centroid of the peak, the main point of interest. Therefore, the Gaussian fit can be used during the energy calibrations.

Each peak in the spectrum was matched to an expected ^{152}Eu peak based on the relative location and height of the peaks. The expected peak energies and intensities were obtained from Ref. [48]. The spectrum peak energies were plotted against the corresponding literature energies and a linear fit was applied, demonstrated in Fig. 4.2. As HPGe detectors tend to have a linear gain, the gain was determined from the gradient of the linear fit. While the energy calibration could be achieved with two peaks, I used eleven peaks as it improved the robustness of the fit. The ^{152}Eu peaks used in the energy calibration are labelled in Fig. 4.3.

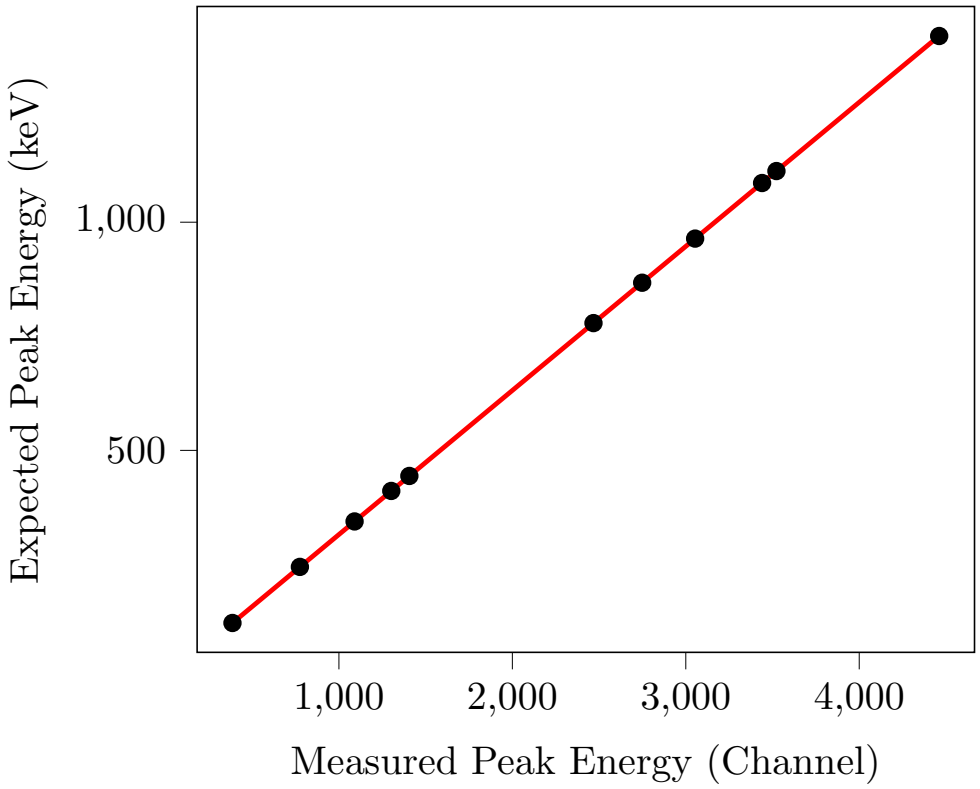

Figure 4.2: Linear fit of the measured peak energies and literature peak energies for the ^{152}Eu source. This was used to calculate the gain on HPGe detector G2.

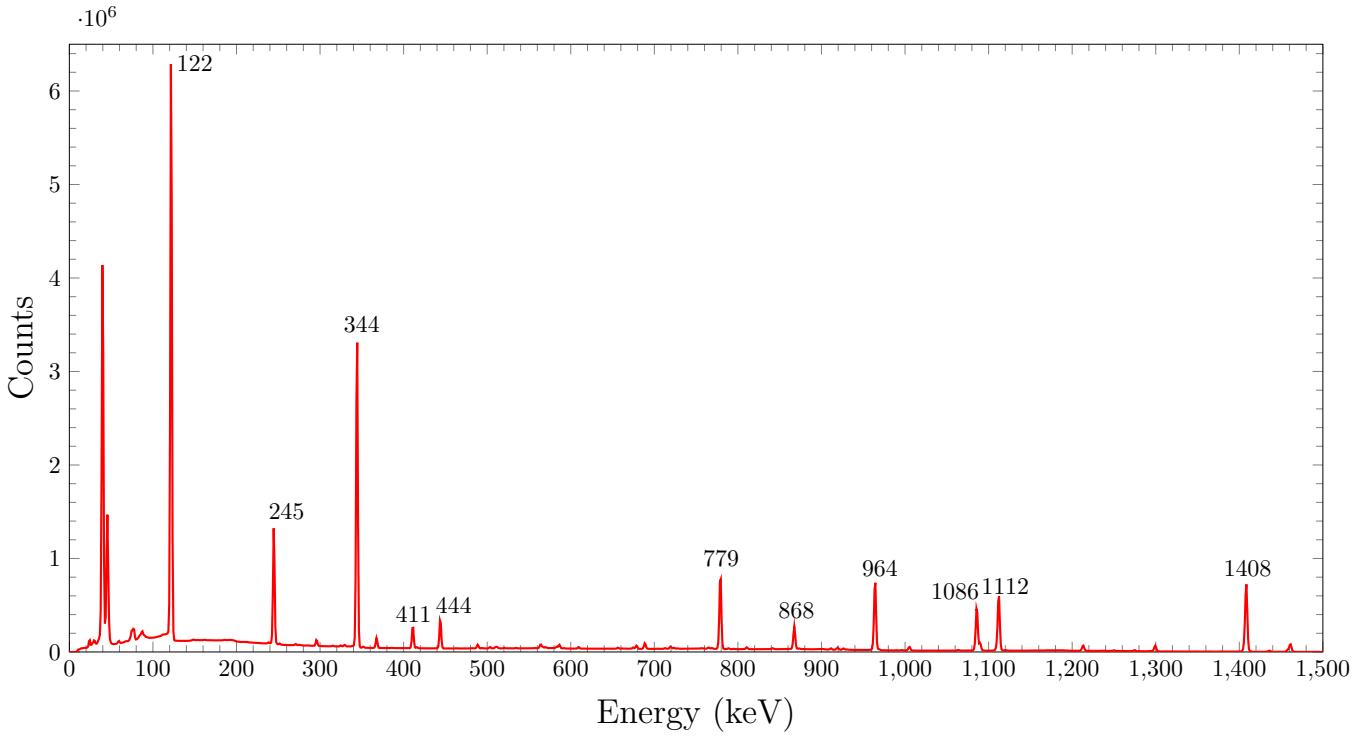

Figure 4.3: A calibrated γ-ray energy spectrum from the ^{152}Eu source. The peaks used for the energy calibration are labelled with energies rounded to the nearest keV.

4.2.2 Doppler Corrections

When ^{121}Sb nuclei undergo Coulomb excitation, they scatter and a portion of the γ decay occurs while the nuclei are in flight. This causes the energy of the γ ray being measured to be Doppler shifted relative to the expected energy. The extent of the Doppler shift is dependent on the lifetime of the excited state. The mean lifetimes of the low-lying excited states of ^{121}Sb range from the order of femtoseconds to nanoseconds. For example, the 37-keV isomer has a lifetime of 4.99 ns, the 573-keV excited state has a lifetime of 14.4 ps and the 1024-keV state has a lifetime of 160 fs [29]. As a result, the target nuclei are in flight when decaying from the short-lived excited states but may be stopped when decaying from the longer-lived states. Therefore, the magnitude of the Doppler shift was determined by the velocity of the recoiling target nucleus when the γ ray was emitted.

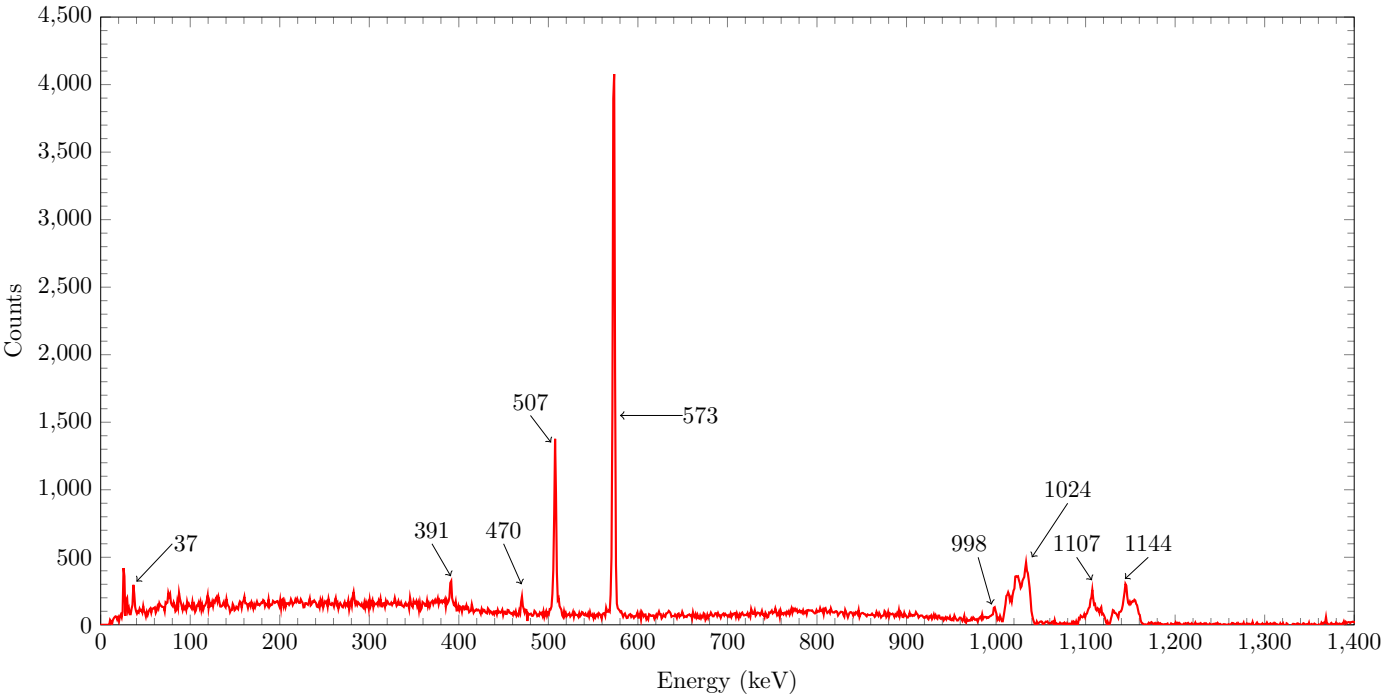

Figure 4.4: The particle-γ energy spectrum summed over all of the HPGe-photodiode pairs for the Coulomb excitation of a 44 MeV ^{16}O beam on an ^{121}Sb target. The identified peaks have been labelled with the energy to the nearest keV. This spectrum has not had a Doppler correction applied to it.

The Doppler shift of the measured peak energy, E_{measured}, relative to the expected energy E_γ is expressed using the equation from [49]

$$\frac{E_{\text{measured}}}{E_\gamma} = \frac{1 + \beta \cos\alpha}{\sqrt{1-\beta^2}}, \tag{4.1}$$

where β is the velocity of the nuclei in units of c and α is the angle between the recoiling target nucleus and the emitted γ ray. The angle α was calculated from the kinematics of the beam. The angle Δ is the angle between the recoiling beam nucleus and the emitted γ ray. This is equal to the angle between the photodiode that detects the beam nucleus and the HPGe detector that detects the γ ray. Using the spherical coordinates of the photodiode and HPGe detector,

$$\cos\Delta = \cos\theta_\gamma \cos\theta_P + \cos(\phi_\gamma - \phi_P) \sin\theta_\gamma \sin\theta_P, \tag{4.2}$$

where θ_P and θ_γ are the polar angles and ϕ_P and ϕ_γ are the azimuthal angles of the

photodiode and HPGe detector respectively. Once Δ was known, the kinematics of the beam were used to calculate α.

Doppler shifts were present in the data, as seen in the 1024-, 1107- and 1144-keV peaks in Fig. 4.4. Doppler shift misaligns the transition peaks between detectors, making it difficult to take fits of the peaks. The peak resolution can be improved by making a Doppler-correction, where the β values are calculated and used to correct the spectrum for Doppler-shift effects. While there are 56 HPGe-photodiode pair combinations, the velocity of the target nuclei is only determined by the photodiode direction. Therefore, each Doppler correction consisted of eight β values.

I calculated the β values using a code developed by PhD student Jack Woodside (**GetBetas**) which fit β values for each photodiode for a specific transition using Eq. 4.1. The expected peak energy along with the range of energies of the peak in the uncorrected ^{121}Sb γ-ray energy spectrum are input into **GetBetas**, which then performs a fit to calculate the β values. An example of a **GetBetas** is presented in Fig. 4.5. As **GetBetas** was only capable of calculating β values for one transition, I repeated the process for three separate transitions.

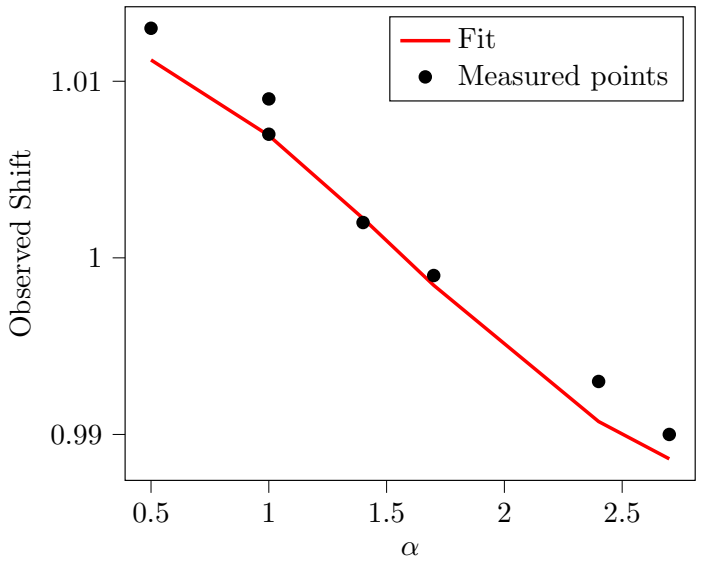

Figure 4.5: A fit produced by **GetBetas** to calculate the β value for photodiode 'A' at the 1024-keV peak. The observed shift represents how far the peak has been Doppler-shifted from the expected value and α is the angle between the recoiling target nucleus and the γ ray. Each measured point represents the Doppler shift in an individual HPGe detector.

The results of the Doppler corrections are presented in Fig. 4.6 and Fig. 4.7. In both spectra, the peak that was Doppler-corrected is sharper compared to the uncorrected spectrum in Fig. 4.4, thereby allowing better fits to be taken when measuring the peak areas. For example, the 1024-keV peak is 34 channels wide in the uncorrected spectrum in Fig. 4.4 and 17 channels wide in the corrected spectrum in Fig. 4.6. However, the Doppler-corrected spectra also illustrated why the Doppler corrections have to be taken for each peak separately. Correcting for the higher-energy peaks introduced energy shift into the lower-energy peaks that was not present in the uncorrected spectrum in Fig. 4.4. Therefore, the Doppler-corrected spectra could only be used to measure the area of a specific peak.

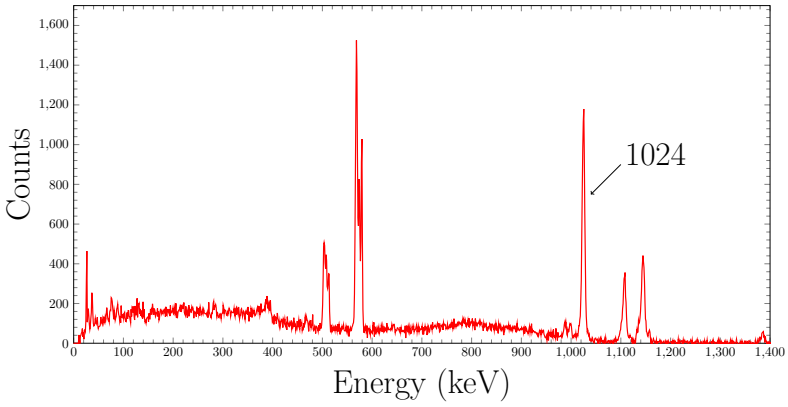

Figure 4.6: A γ-ray spectrum of the ^{121}Sb target Doppler-corrected around the 1024 keV peak. The higher energy peaks are much sharper, allowing for more accurate fits to get the counts under the peak The lower-energy peaks are less defined compared to the uncorrected spectrum.

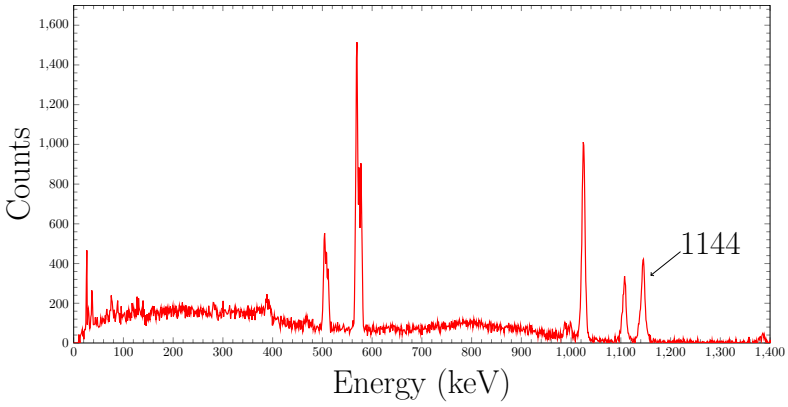

Figure 4.7: A γ-ray spectrum of the ^{121}Sb target Doppler-corrected around the 1144 keV peak. The higher energy peaks are much sharper, allowing for more accurate fits to get the counts under the peak.

4.2.3 Particle Detector Calibrations

Timing and energy gates were applied to the particle detectors to remove contaminants from the spectra and align the timings of the particle detectors and the HPGe detectors. The particle-energy spectra, such as the example in Fig. 4.8, include both particles emitted from the target and contamination by other particles such as electrons. The contaminant particles were at a lower energy than the target particles and were eliminated by applying software energy gates to the particle energy spectra. The gates performed an energy cut and only included events within the gates when resorting the data. The particle region and the contaminant region of the spectra did not overlap, so there was no chance of including contaminants in the final γ-ray spectrum. Initially, **CaesarSort** was hard coded to apply one specific particle-energy gate. As a result, the gain of the particle-energy spectra had to be adjusted to ensure the particle-energy distribution for each photodiode fit within one set of gates. This had the consequence of losing coincidence events as each particle-energy distribution had a different shape. Improvements to **CaesarSort** in 2024 made by J. Woodside enabled individual energy gates to be set for each particle detector, allowing for energy gates that fit the different energy distributions.

Timing gates were also applied to identify coincidences between the photodiodes and HPGe detectors. The time-difference spectrum between a particle detector and γ-ray detector had one main peak representing 'real' coincidence events and a background representing 'random' coincidence events, as shown in Fig. 4.9. A software timing gate needed to be applied to align the detectors in time and a random subtraction also had to be performed due to the prominence of uncorrelated events. This required placing a main gate around the peak in the time-difference spectrum and two background gates on either side of the peak. Unlike the particle-energy spectra, **CaesarSort** only allowed for one specific particle-γ timing gate to be applied. Therefore, the time-offset of every particle detector was adjusted so that the main coincidence peak was centred around zero to fit within the timing gates.

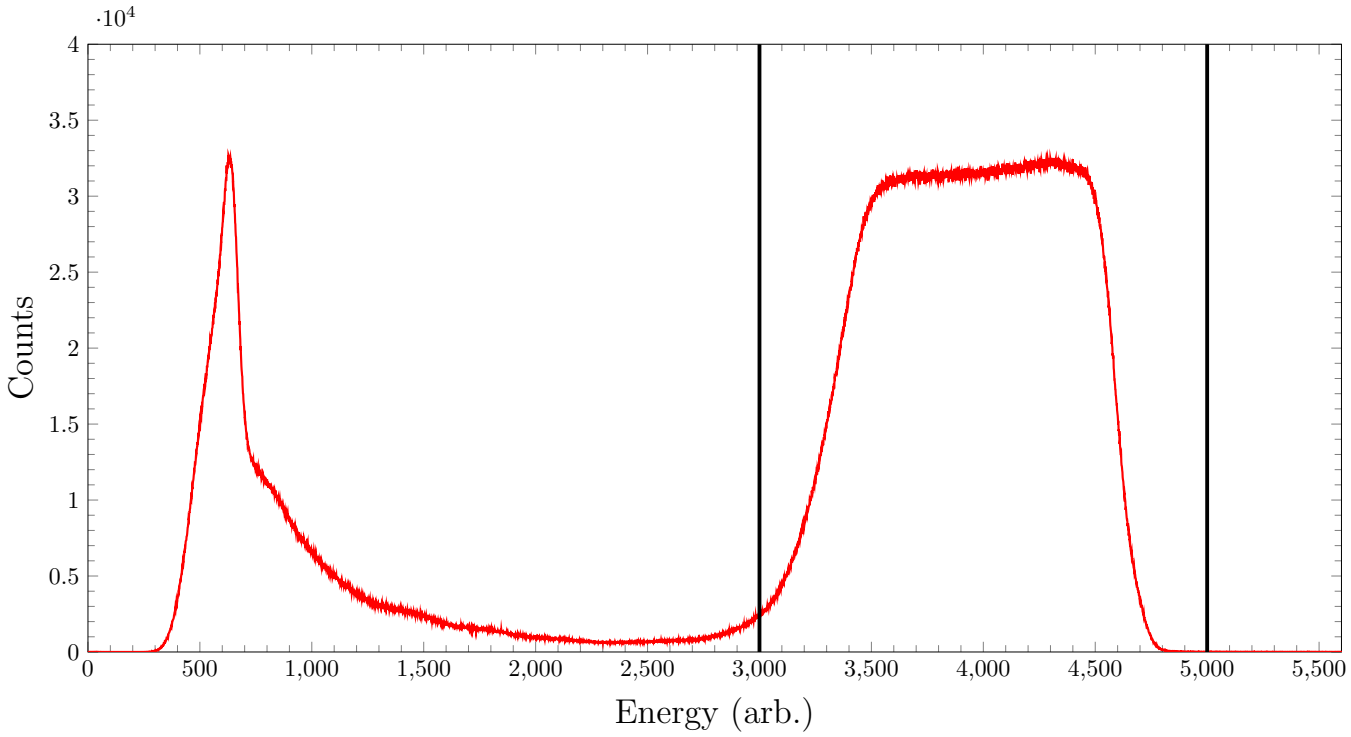

Figure 4.8: The particle energy spectrum for photodiode 'B' summed over the entire experiment. The spectrum was gated around the higher end of the energy range to remove contaminants from the spectrum. The gates are marked by black lines.

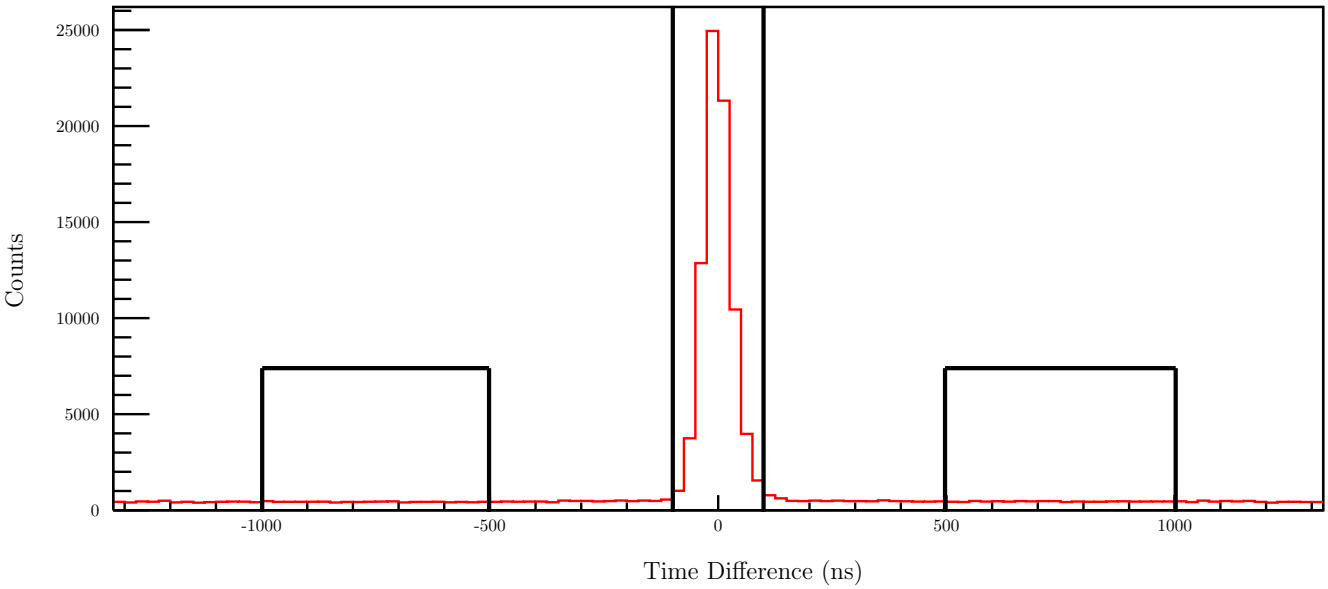

Figure 4.9: The time-difference spectrum between HPGe G6 and photodiode 'C', summed over the entire experiment. Timing and background gates are marked by black lines.

4.2.4 Peak Area Measurements

The HPGe γ-ray detectors used in this experiment have energy resolutions on the order of a single keV. As a result, the transition peaks have near-Gaussian energy distributions in the spectra. The peaks have a tail at the low end of the distribution due to the incomplete energy deposition of the γ ray into the germanium crystal, as illustrated in in Fig. 4.10. The near-Gaussian shape of the peaks was also a result of Doppler shifts discussed in Section 4.2.2. The Doppler-shifting of the γ rays increased the range of energies of γ rays emitted during a specific decay, leading to the peak becoming wider. As a result of these factors, the peaks do not have Gaussian shapes and so a Gaussian fit would not give an accurate measurement of the peak area.

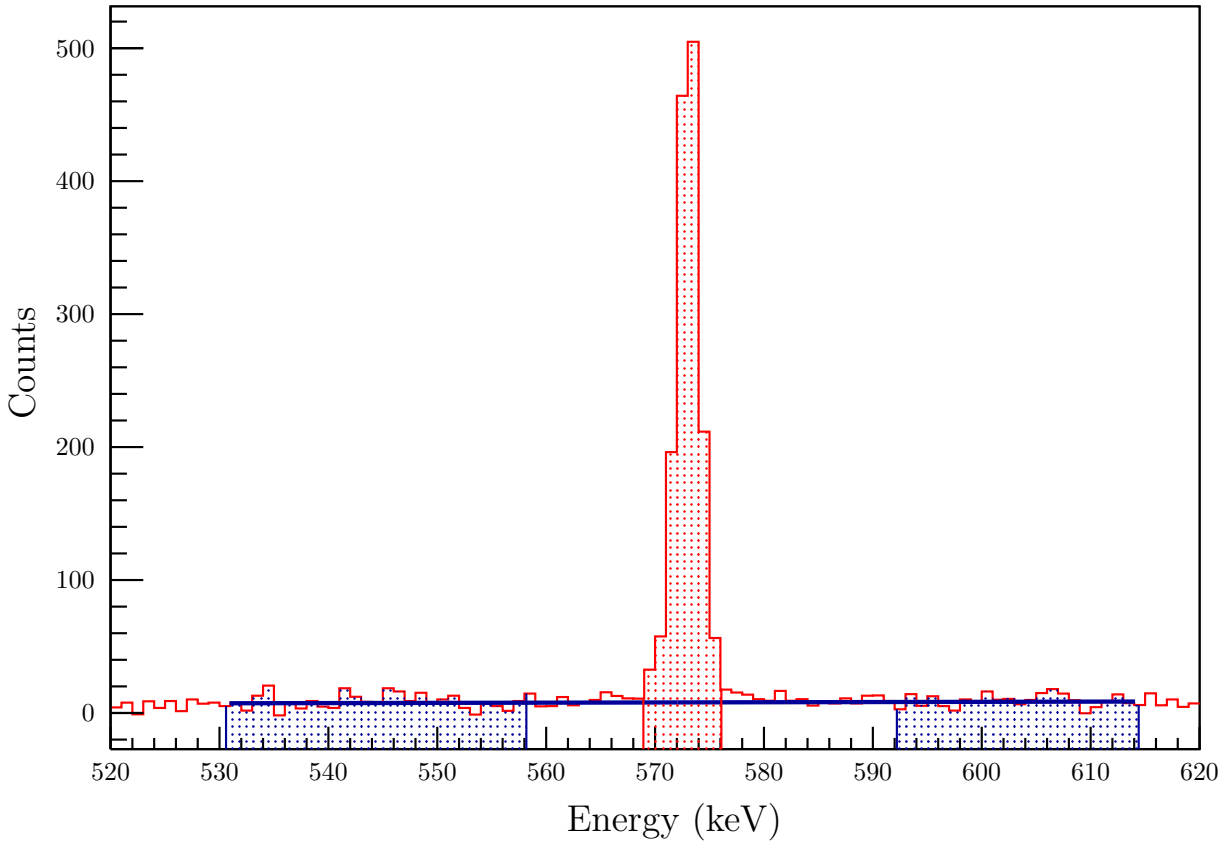

Figure 4.10: A fit using the sum over background method on the 573 keV peak for the energy spectrum of photodiode 'A' summed over all of the HPGe detectors. The red region is the peak and the blue regions are the backgrounds.

An alternative method to fitting Gaussian functions used was the 'sum over back-

ground' method. In this method, an energy gate is placed around the peak and two background regions are defined on either side of the peak. An integration sum of the peak region is taken and the background regions are subtracted from the sum to give a peak area measurement. The sum over background method was independent of peak shape, which improved its accuracy for non-Gaussian peak. The main limitation of the sum over background method is that it is difficult to fit overlapping peaks. However, the ^{121}Sb spectra did not feature any overlapping peaks, so this was not an issue when measuring the peak areas.

4.2.5 Efficiencies

Another correction that needed to be performed on the yields is correcting for the detection efficiency. The efficiency of the detectors was dependent on the energy of the γ rays so the yields of each transition had to be corrected separately. The efficiency correction was performed by calculating the relative efficiencies of the peaks of the three calibration sources. A relative efficiency curve was fit to the data points and then scaled to produce absolute efficiency curves. The three calibration sources were all used in calculating the efficiencies as the peaks provided a wide range of energies that improved the fit accuracy, especially in the energy range below 100 keV.

HPGe detector efficiency increases exponentially until it peaks at around 200 keV and then exponentially decreases. The transition from the isomer state was below this energy and the other ^{121}Sb transitions of interest were significantly above this turnover point. A function describing the relative efficiency as a function of energy, $\eta_{\text{rel}}(E)$, was fit to the relative efficiencies of the calibration sources. I used the fitting function [50]

$$\eta_{\text{rel}}(E) = \exp\left\{\left[\left(a_0 + a_1 x + a_2 x^2\right)^{-C} + \left(b_0 + b_1 y + b_2 y^2\right)^{-C}\right]^{-\frac{1}{C}}\right\}, \tag{4.3}$$

where a_i, b_i and C are fitting parameters, $x = \ln\left(\frac{E}{100}\right)$ and $y = \ln\left(\frac{E}{1000}\right)$.

An initial fit was performed to test the fitting function using the ^{152}Eu source. Europium-152 was selected for initial fit as it was also the only calibration source that the function could fit to by itself. This was because the ^{133}Ba and ^{207}Bi sources did not have enough peaks to take a fit of the efficiency function. I included nine ^{152}Eu γ-ray peaks as

well as the two europium x-ray peaks produced during internal conversion. The x-rays had energies of the order of 10 keV so they improved the fit in the energy region below 100 keV. I determined relative efficiency of the ^{152}Eu peaks by measuring the peak areas using the sum over background method described in Section 4.2.4 and then divided the peak areas by the relative intensities obtained from Ref. [48]. A initial relative efficiency curve was produced for each HPGe detector, an example of which is presented in Fig. 4.11. Once the initial fits were taken, the process of calculating the relative efficiencies was repeated for the ^{133}Ba and ^{207}Bi peaks using intensity data obtained from Ref. [51] and Ref. [52]. However, as the relative efficiencies were at an arbitrary scale, the absolute efficiencies of the three sets of calibration data had to be calculated so that an absolute efficiency fit could be performed.

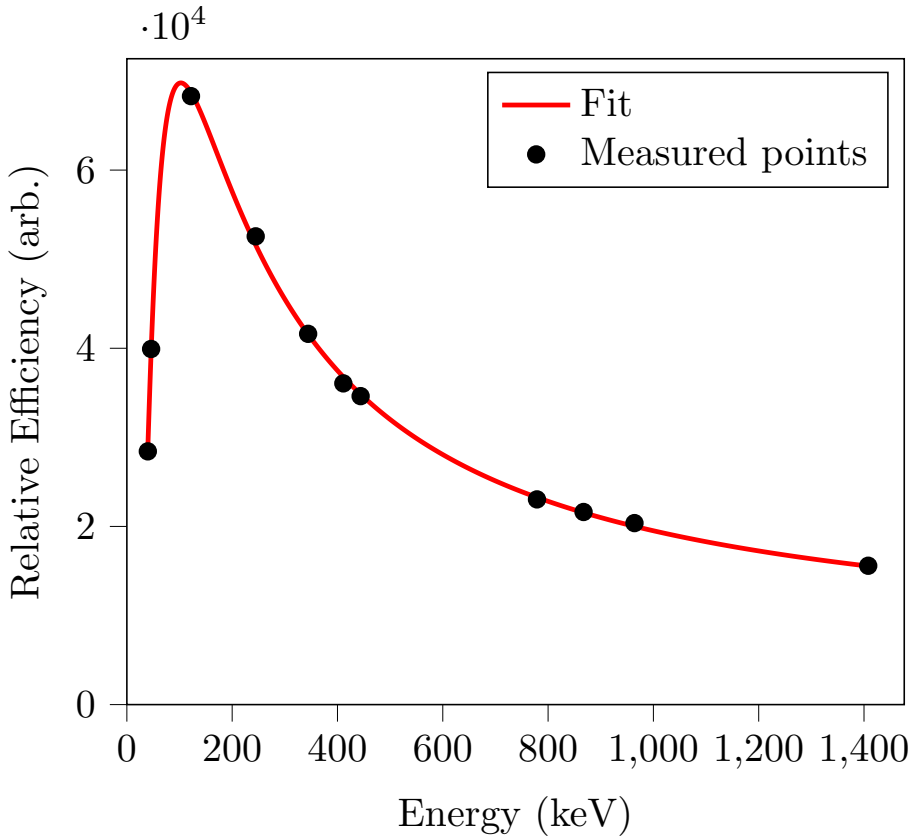

Figure 4.11: An initial fit of the relative efficiency curve for the ^{152}Eu source in HPGe detector G2. Uncertainties were determined from the background subtraction method but are too small to be seen at this scale.

Absolute Efficiencies

The absolute detector efficiencies were calculated by measuring the γ-ray cascade from the calibration sources. A cascade in γ decay is where a transition from level A to level B is followed by a transition from level B to level C, illustrated in Fig. 4.12. As a result, two γ rays, γ_1 and γ_2, are emitted in series and detected by different detectors [53].

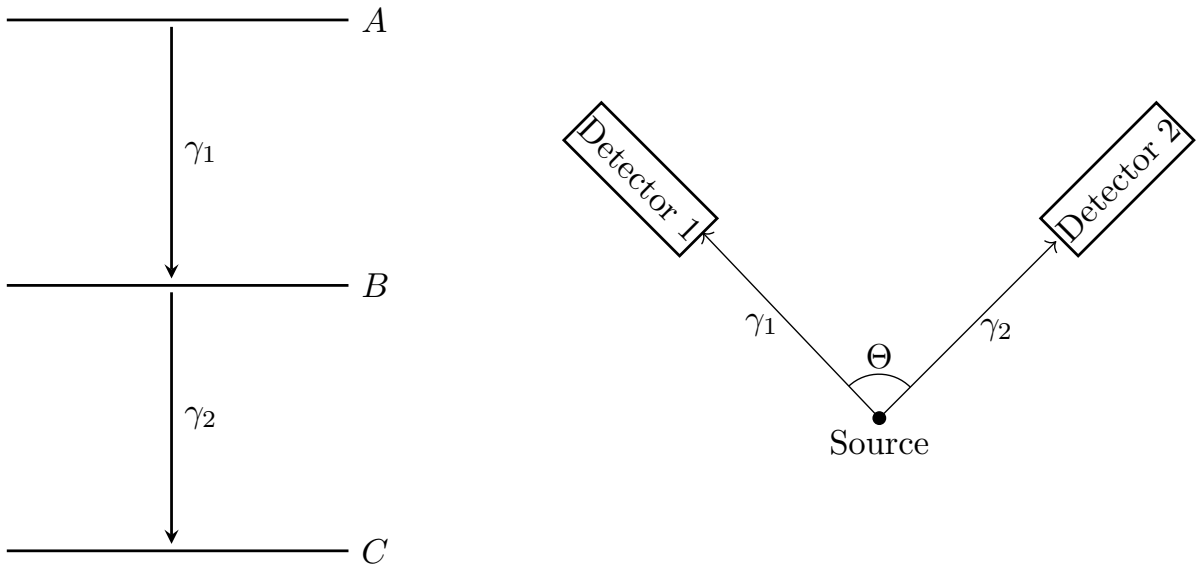

Figure 4.12: A level scheme showing a γ-ray cascade (left). The two γ rays are emitted from a source and detected by different γ-ray detectors separated by angle Θ (right).

The number of γ_1 events recorded by Detector 1 is

$$N_1 = N_{\gamma_1}\eta_1, \tag{4.4}$$

where N_{γ_1} is the actual number of γ rays that reached Detector 1 and η_1 is the absolute efficiency of Detector 1. The number of γ_2 events recorded by Detector 2 in coincidence with Detector 1 is

$$N_{2,1} = p_2 N_1 \eta_1 \eta_2 W(\Theta), \tag{4.5}$$

where p_2 is the probability of γ_2 being emitted, η_2 is the absolute efficiency of Detector 2 and $W(\Theta)$ is the γ-γ angular correlation term that will be discussed later. Combining Eq. 4.4 and Eq. 4.5 and accounting for internal conversion gives the absolute efficiency

of Detector 2 as

$$\eta_2 = \frac{N_{2,1}}{N_1 p_2} \frac{(1+\alpha)}{W(\Theta)}, \tag{4.6}$$

where α is the internal conversion coefficient. Therefore, the absolute efficiency of Detector 2 at the energy of γ_2 can be calculated by taking the ratio of $N_{2,1}$ and N_1 and scaling by the probability of γ_2 and the angular correction factor.

The cascade method was performed using the ^{207}Bi source. Bismuth-207 undergoes electron capture and decays to a ^{207}Pb nucleus in a 1633-keV excited state. The ^{207}Pb nucleus then undergoes a 1063-keV decay transition followed by a 569-keV decay transition to its ground state [51].

The cascade method was performed by sorting the calibration source data using **CaesarSort** to produce γ-γ coincidence spectra. The sum over background method was used to get the 569-keV coincidence areas by gating around the 1063-keV peak and then measuring the 569-keV peak area. This process was repeated for each HPGe-HPGe detector combination. As there were seven HPGe detectors and a detector cannot be in coincidence with itself, I had six data points per detector. I averaged the result to get an absolute efficiency at 569 keV for each HPGe detector and took the standard deviation as the uncertainty. The absolute efficiency at 569 keV was used to convert the relative efficiency data to absolute efficiencies.

Initially, the ^{207}Bi cascade was used to scale all of the calibration data to absolute efficiencies. However, the ^{133}Ba data was not in agreement with the other sources, which caused the fitting code to fail. This was resolved by applying the cascade method to each source separately. The ^{152}Eu cascade was a 1408-keV transition into a 122-keV transition and the ^{133}Ba cascade was a 356-keV transition into a 81-keV transition. This aligned the data correctly and produced absolute-efficiency functions for each HPGe detector, an example of which is shown in Fig. 4.13.

Another issue was fitting the low-energy region of the absolute efficiency curves. The fitting function Eq 4.3 was numerically unstable at low energy values and combining the ^{152}Eu, ^{133}Ba and ^{207}Bi data would break it due to this instability. The issue of numerical instability at low energy was solved by implementing an algorithm provided to me by Professor Greg Lane. The algorithm performed the fit in stages, first by calculating

the a_i and b_i parameters separately. It would then check the difference between the $a_0 + a_1x + a_2x^2$ term and the $b_0 + b_1y + b_2y^2$ term in Eq. 4.3. If the difference between the terms was greater than six orders of magnitude, the code would fit the exponent of the smaller term. Otherwise, the code would fit the data to the form of Eq. 4.3.

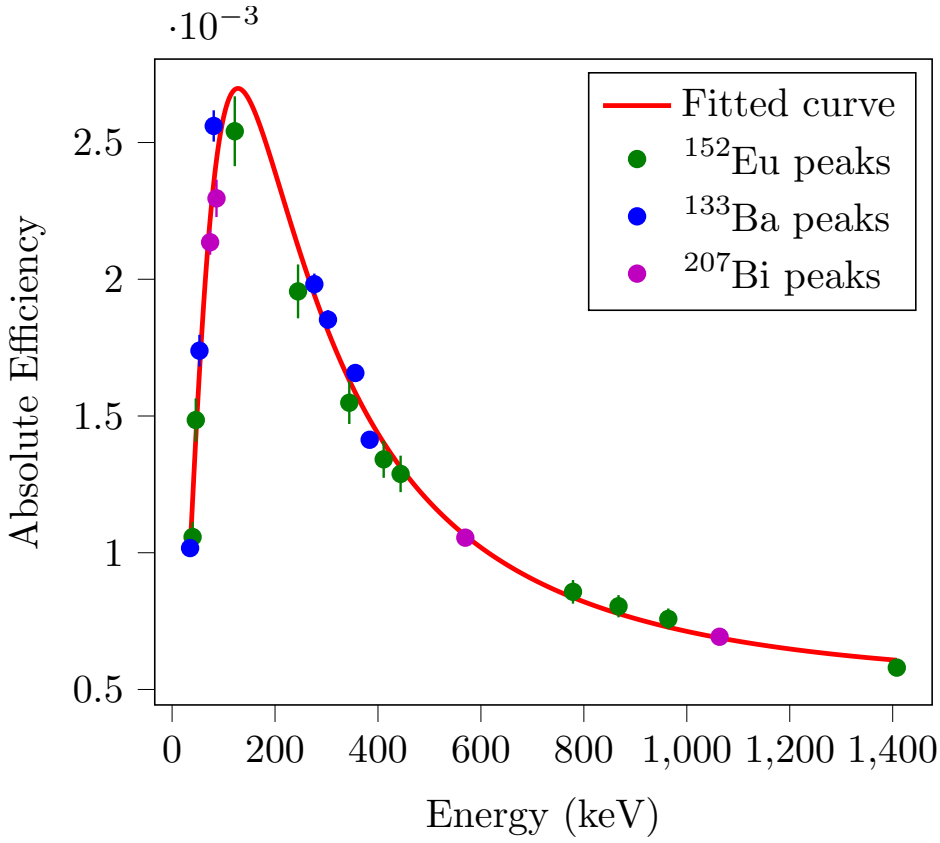

Figure 4.13: Absolute efficiency curve fit to all three calibration sources in HPGe detector G2. Uncertainties were determined from the sum over background method used to get the yields but some uncertainties were too small to be seen at this scale.

γ-γ Angular Correlations

The cascade method relies on the two γ rays in the cascade being detected by different detectors separated by an angle Θ. As a result, the absolute efficiency correction includes a γ-γ angular-correlation term $W(\Theta)$ to account for the difference in angle between the HPGe detectors. The angle between the two detectors Θ with angle positions (θ_1, ϕ_1) and (θ_2, ϕ_2) respectively is expressed as

$$\cos\Theta = \cos\theta_1 \cos\theta_2 + \cos(\phi_1 - \phi_2) \sin\theta_1 \sin\theta_2. \tag{4.7}$$

The angular-correlation factor can be expressed as

$$CW(\Theta) = \frac{N_{2,1}}{N_1 N_2}, \tag{4.8}$$

where N_2 is the number of γ_2 events detected independent of γ_1 events and C is a constant. The values of $CW(\Theta)$ were calculated using Eq 4.8 and the results were plotted against Θ for each HPGe-HPGe combination. The data points were fitted to a trigonometric polynomial function [14]

$$CW(\Theta) = 1 + \sum_{k=1}^{L} a_{2k} \cos^{2k}(\Theta), \tag{4.9}$$

as illustrated in Fig. 4.14.

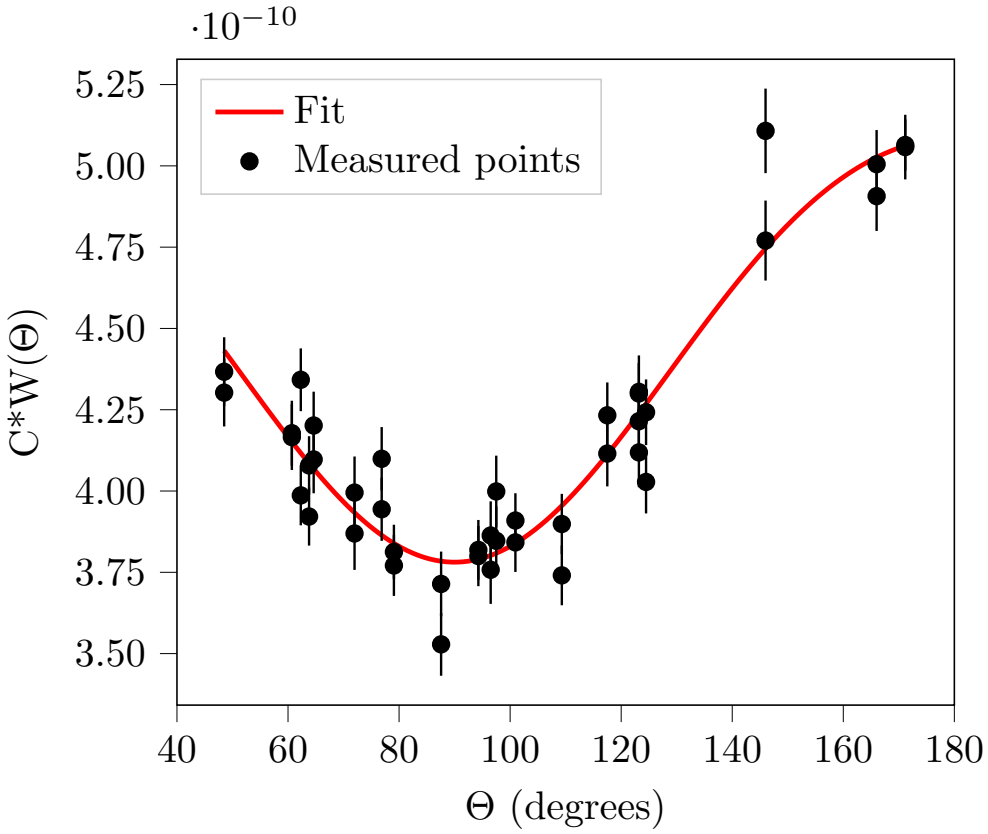

Figure 4.14: The γ-γ angular correlation curve for the ^{207}Bi data. Unlike the efficiency curves, the angular correlation is fit to all HPGe-HPGe detector combinations simultaneously.

The fit was used to determine the values of C and a_{2k} up to $L = 2$. This gave $W(\Theta)$

a functional form which could be used to calculate the $W(\Theta)$ value for each HPGe-HPGe combination. The values of $W(\Theta)$ varied depending on calibration source. The ^{152}Eu and ^{207}Bi angular corrections ranged from 1.0 to 1.3 while the ^{133}Ba angular corrections had a smaller variance of between 1.0 and 1.1.

4.3 γ-Ray Yields

4.3.1 Yield Corrections

Once the particle-gated γ-ray spectra were calibrated and the absolute detection efficiencies were calculated, the overall yields for each individual particle detector could be determined. The yields were determined by measuring the peak areas using the sum over background method. Those measurements then needed to be corrected for factors such as angular correlations and HPGe detector efficiency as discussed previously. For a given particle detector, the total yield of a peak across a 4π solid angle is given by

$$\text{Yield}(E_\gamma) = N \left\{ \sum_{\text{HPGe}} \left[\eta_{\text{rel}}(E_\gamma) \times \frac{\eta_{\text{abs}}(E_{\text{cascade}})}{\eta_{\text{rel}}(E_{\text{cascade}})} \times W(\theta_\gamma, \Delta\phi) \right] \right\}^{-1} \tag{4.10}$$

where N is the number of counts, equivalent to the peak area, and $W(\theta_\gamma, \Delta\phi)$ is the particle-γ angular correlation factor.

Particle-γ Angular Correlations

When an excited nucleus emits a γ ray, the spin of the initial excited state influences the direction of the trajectory of the γ ray. The distribution of spin alignment in the target nuclei is related to the particle scattering angle, while the radioactive calibration sources have no spin alignment. However, when using the cascade method, the alignment of the middle state was determined by the direction of the first γ ray, which affects the directional distribution of the second γ ray.

The γ-ray yield averaged over the full 4π solid angle range for each photodiode needs to be discerned in order to calculate the Coulomb excitation cross-section. This was done by correcting the measured yields for each photodiode-HPGe pair for deviations from the

average yield across the full solid angle.

The angular distribution of γ rays after Coulomb excitation is given by the function [54, 55]

$$W(\theta_P, \theta_\gamma, \Delta\phi) = \sum_{kq} B_{kq}(\theta_P) Q_k F_k G_k D^{k*}_{q0}(\Delta\phi, \theta_\gamma, 0), \tag{4.11}$$

where $\Delta\phi$ is the difference in azimuthal angle between the particle and γ-ray detector. For $E2$ and mixed $M1 + E2$ transitions, $k \in \{0, 2, 4\}$ and q can take on integer values from $-k$ to k.

The $B_{kq}(\theta_P)$ term is the statistical tensor which determines the initial spin alignment and can be calculated for a specific angle using knowledge of reaction dynamics [55]. The tensor must be integrated over the range of possible scattering angles, which in this experiment was the rectangular surface of the photodiodes.

The Q_k terms account for the solid-angle attenuation from the finite shape of the γ-ray detectors. The BGO Compton suppressors limit the HPGe opening angle so it was assumed that $Q_k = 1$.

The F_k terms contain information about the initial and final spin states. These can be found in various tables [56].

The G_k terms account for the vacuum deorientation effect. When a nucleus recoils into a vacuum, the $B_{kq}(\theta_P)$ changes over time in relation to the nuclear g-factor. The time-dependent G_k terms can be expressed as

$$G_k(t) = e^{-\lambda_k t}, \tag{4.12}$$

where λ_k is the vacuum orientation rate. Integrating over time t gives the G_k terms as

$$G_k = \frac{1}{1 + \lambda_k \tau_N}, \tag{4.13}$$

where τ_N is the state mean lifetime [57]. The $D^{k*}_{q0}(\Delta\phi, \theta_\gamma, 0)$ terms are the Wigner-D matrices.

For the described analysis in this thesis, I used **Gosia** to calculate the angular correlation term. I simulated a Coulomb-excitation interaction of ^{16}O on ^{121}Sb at 44 MeV for both a single detector with a 4π solid angle and the CAESAR array used in the exper-

iment. The input levels, transitions and matrix elements were obtained from Ref. [29]. The yields output by **Gosia** were used to calculate $W(\theta_\gamma, \Delta\phi)$ term through dividing the yields from the CAESAR simulation by the yields from the 4π-detector simulation.

4.4 Gosia

Gosia is a program designed to analyse large volumes of data from Coulomb-excitation experiments [38]. It is able to fit transition matrix elements to experimental yields. **Gosia** is based on the Winther-de-Boer code [58] that uses a semi-classical theory of Coulomb excitation to calculate expected γ-ray yields from matrix elements.

4.4.1 Inputs

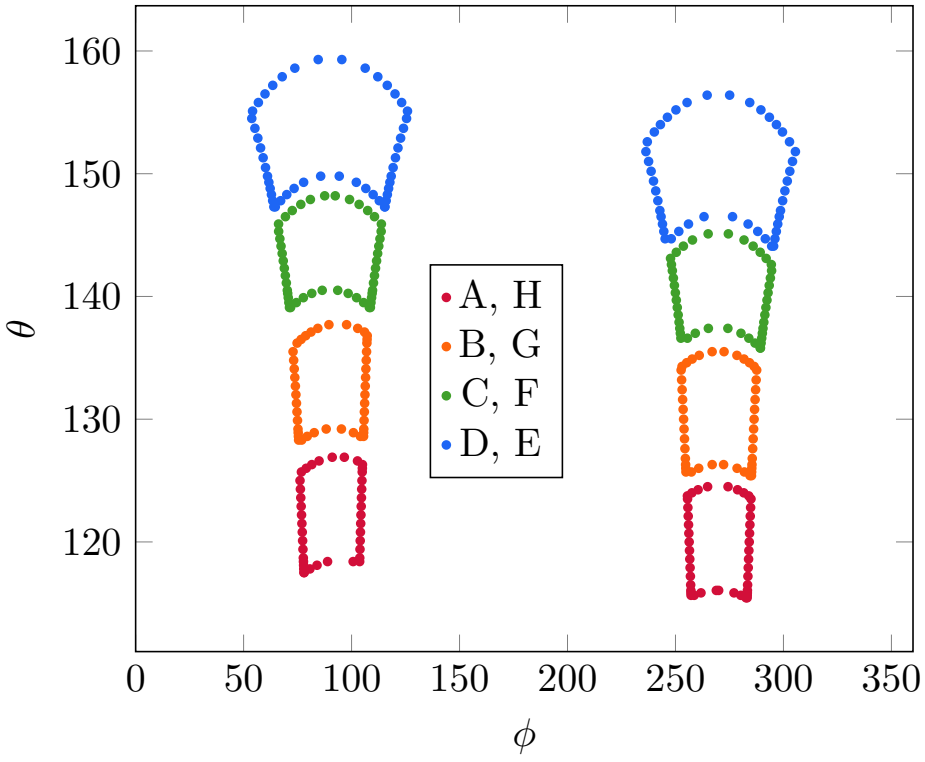

Figure 4.15: The positions of the photodiodes in spherical coordinates that were used in the **Gosia** input file. Photodiodes 'A' to 'D' are on the left and photodiodes 'E' to 'H' are on the right. Figure created by J. Woodside and reproduced with permission.

Gosia takes a variety of inputs to define both the experimental conditions and the structure of the nuclei. Properties of the nuclear states such as energy, spin and parity have

to be specified, as well as the transition matrix elements for each multipolarity. The initial matrix elements have to be guessed, though the guess can be informed by previous experimental data. The allowed range of the matrix element in the fitting has to be defined or alternatively the matrix element can be fixed. Other properties of the nucleus, such as the branching ratio of two transitions, the mixing ratio of a mixed transition and mean state lifetimes, were optional inputs but provided more constraints for the fitting process. Internal conversion coefficients were calculated through the BrIcc database [59]. Experimental conditions also needed to be input, including a set of energies for **Gosia** to integrate over, the spatial coordinates of the detectors and the experimental γ-ray yields. The lower value of the energy set was the full energy loss in the target, which was calculated using a code developed by Professor Andrew Stuchbery. The upper value was the energy of the beam.

The γ-ray detector angular positions were fixed while the particle detectors had a range of ϕ values for every θ value. These were input as a list of θ values and a range of ϕ for each particle detector. The possible (θ, ϕ) combinations for each photodiode are displayed in Fig. 4.15. Other inputs included the stopping powers which were used to define the target thickness. I calculated the stopping powers from the set of energies using SRIM, a software packages which calculates the energies of interactions of ions in matter [60]. The experimental yields for each particle detector, calculated using Eq. 4.10, were input with uncertainties into **Gosia** to be used in the fitting process.

4.4.2 Fitting and Outputs

Gosia calculated the excitation cross-sections from the given initial matrix elements using the Winther-de Boer code. The excitation cross-sections are then used by **Gosia**, alongside the input parameters to calculate the γ-ray yields through an iterative process of recalculating the cross sections to vary the matrix elements. During the fitting process, Gosia outputs a χ^2 parameter which represents the differences between the inputs and the calculated outputs. The fitting stops when the χ^2 parameter reaches a local minimum. **Gosia** then outputs the fitted matrix elements, yields calculated from those matrix elements and other results from the fit such as branching and mixing ratios. The

output also included a comparison between the calculated and expected values of each input parameter. The fitted yields were then compared to the experimental yields to evaluate the accuracy of the fit. The fitting process was repeated with different input matrix elements to improve the alignment between the experimental and fitted yields.

4.5 Analysis Approach

The analysis is described in detail in Chapter 5. The experimental yields were normalised and compared to the yields produced by the **Gosia** fits. The accuracy of the **Gosia** fits was determined by how many fitted yields were within uncertainty of the experimental yields. The initial matrix elements were varied to improve the quality of the fits. Once I was satisfied with the agreement between the experimental yields and the fitted yields, I used the fitted matrix elements generated by **Gosia** to calculate the $B(E2)$ values for each transition and compared them to the literature values.

Chapter 5

Results

In this chapter, I will discuss the results of my analysis. First, I identified transitions of ^{121}Sb in the γ-ray spectra and measured the areas of those transition peaks (Section 5.1). I applied the correction factors to calculate the γ-ray yields from the peak areas (Section 5.2). This enabled me to verify the analysis method by comparing the final yields between particle detectors (Section 5.3). I will then discuss the results of fitting **Gosia** yields to the experimental yields (Section 5.4). Finally, I will discuss the $B(E2)$ values and state mean lifetimes calculated from the fitted matrix elements and compare them to literature values (Section 5.5).

5.1 Identified ^{121}Sb Transitions

Nine transitions of ^{121}Sb were observed in the γ-ray spectra and are labelled in Fig. 4.4. The level scheme in Fig. 5.1 shows where the identified transitions are located in the structure of ^{121}Sb. Some of the identified transitions were not be included in the analysis due to low statistics. The $11/2_1^- \rightarrow 9/2_2^+$ transition was visible on the combined spectrum at 391 keV but was only visible above background on two of the individual particle-detector spectra. The $11/2_1^- \rightarrow 9/2_4^+$ transition was only visible on the spectrum for particle detector 'E' and was not visible above background on the combined spectrum, so it was not labelled in Fig. 4.4. The low statistics made it difficult to distinguish the peak from the background and thus the peak area for the 282-keV and 391-keV peaks could not be reliably measured. Without peak area measurements, the experimental yields were not able to be calculated and thus the 282-keV and 391-keV peaks were not included in the **Gosia** fitting process.

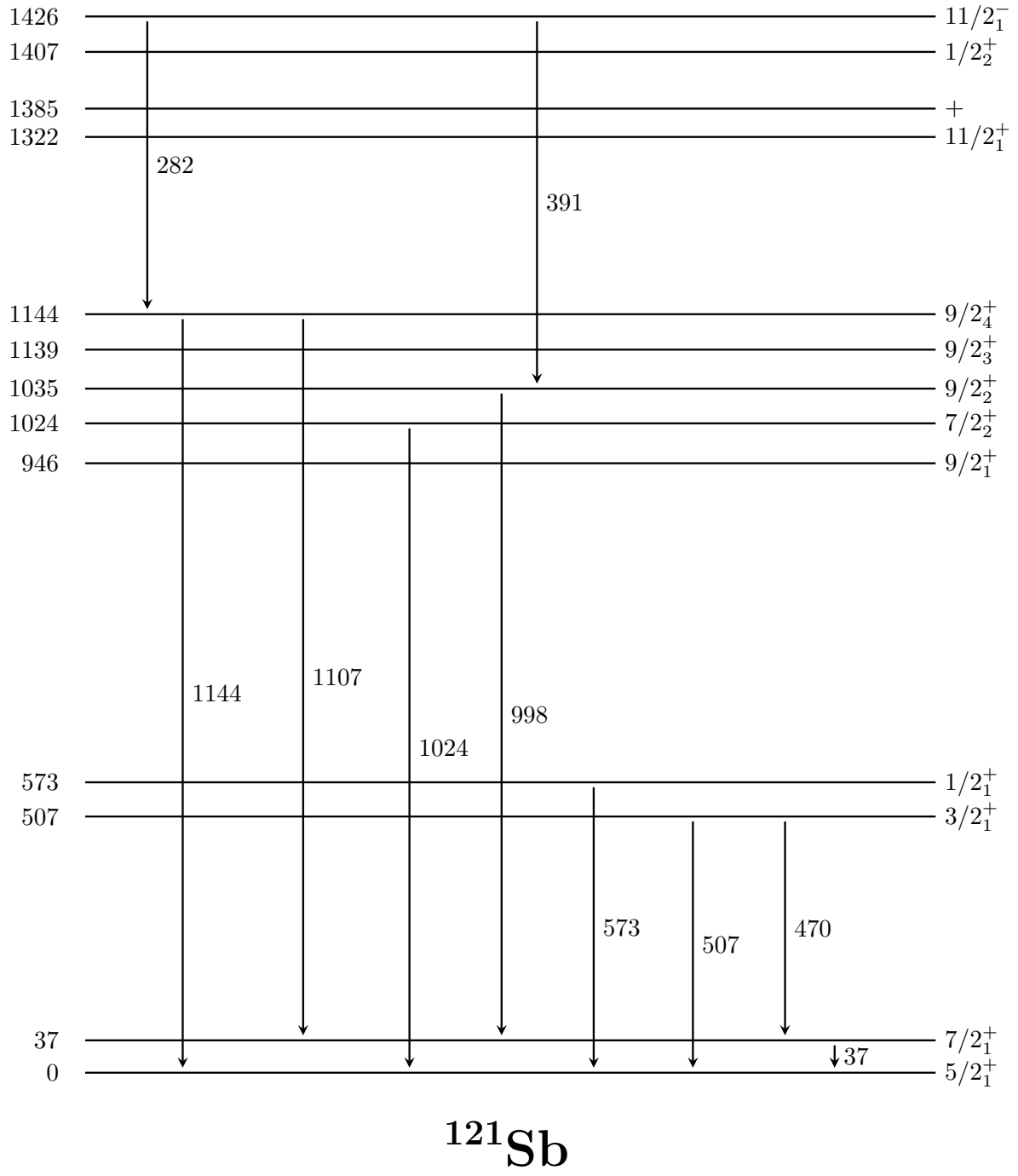

Figure 5.1: Level scheme of ^{121}Sb showing transitions that were identified in the experiment. The excited state energies are labelled with energies to the nearest keV on the left and spin-parity on the right. Excited state energies and spin-parities obtained from Ref. [29]. Note that the 1385-keV excited state did not have an assigned spin as of the publication of Ref. [29]. The transitions are labelled with energy to the nearest keV. The $7/2_1^+$ state is the isomer of interest for the isomer power program.

5.2 Correction Factors

5.2.1 Absolute Efficiency

I calculated the absolute-efficiency correction using the cascade method described in Section 4.2.5 for each calibration source. Initially, I used the ^{207}Bi cascade to correct for all three sources but the ^{133}Ba data points were found to be inconsistent with the relative the efficiency curve. This was problematic because the focus of this thesis was on low-energy Coulomb excitation, particularly the 37-keV transition from the $7/2_1^+$ isomer to the ground state. Barium-133 was the only calibration source to have a peak below 37 keV. Therefore, the ^{133}Ba data had to be included to ensure the efficiency curve was accurate for all ^{121}Sb peaks. To resolve this issue, I performed the cascade method on each source individually, which aligned the three sources and enabled me to fit an absolute efficiency curve for each HPGe detector.

5.2.2 Angular Correlations

I calculated the angular correlations using **Gosia** to simulate the Coulomb-excitation yields. To do so, I calculated matrix elements using ^{121}Sb transition probability data from Ref. [29] and input them into **Gosia**. The first simulation assumed a single detector with 4π coverage, similar to my tests described in Section 2.7, while the second simulation used the positions of the HPGe detectors in CAESAR. This enabled me to calculate the angular correlation factor for each transition in each HPGe-photodiode pair. The angular correlation factor $W(\theta, \Delta\phi)$ ranged between 0.9 and 1.1 for the different HPGe-photodiode combinations.

5.2.3 Final γ-ray Yield Corrections

I calculated the absolute efficiency and angular correlation factors using the methods discussed in Section 5.2 and further elaborated on in Chapter 4. I was able to use the sum over background method to measure the yields of eight of the identified transitions and applied the correction factors to get the final γ-ray yields using Eq 4.10.

5.3 Comparison of Experimental Yields

To check the efficiency calibration and angular correlation of the measured γ-ray yields, I compared the experimental yields between each particle detector. When the correction factors are applied and the yields are normalised relative to a chosen transition, the yield for a specific transition should be the same in each particle detector. I normalised the yields of the observed transition to the $1/2_1^+ \rightarrow 5/2_1^+$ transition, as that transition had the highest number of yields. An example of comparing the normalised experimental yields is illustrated in Fig 5.2. Most of the normalised experimental yields for each transition agreed within uncertainty across the particle detector array. The only notable outlier was the $3/2_1^+ \rightarrow 5/2_1^+$ transition yield in particle detector 'B' which had higher yields compared to the other detectors. This was most likely due to an over count as the measured peak areas in the detector 'B' spectrum tended to be lower than the other particle detectors.

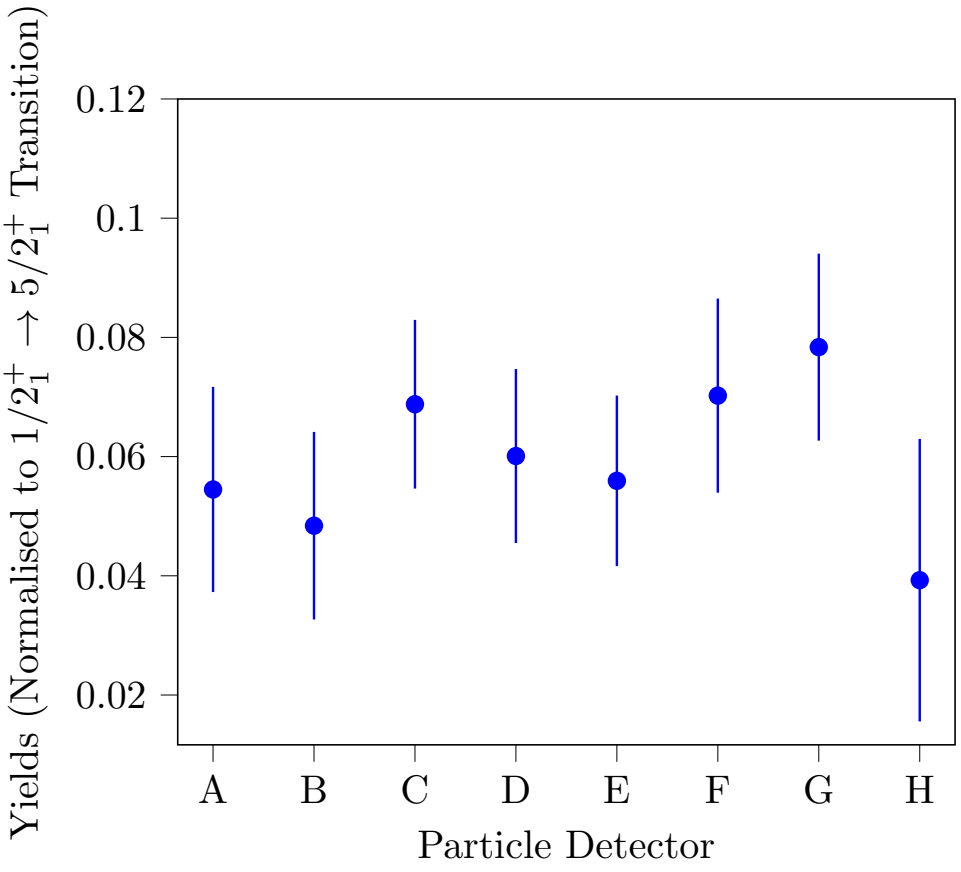

Figure 5.2: Comparison between the experimental yields of the $7/2_1^+ \rightarrow 5/2_1^+$ transition for each particle detector.

5.4 ^{121}Sb Results

5.4.1 Yield Measurements

The areas of the other identified peaks were obtained using the sum over background method described in Section 4.2.4. The higher-energy peaks exhibited Doppler shifts which made fitting difficult. This was resolved by correcting for Doppler shifts as discussed in Section 4.1 around the 1024 keV, 1107 keV and 1144 keV peaks individually. This gave the peaks better definition, which allowed for better fits using the sum over background method. The correction factors were applied to produce the γ-ray yields, which were input into **Gosia**.

5.4.2 Initial Values for Matrix Elements

The initial matrix elements for the Gosia fits were calculated using literature values of the $B(E2)$ and $B(M1)$ values obtained from Ref. [29]. The matrix elements were obtained from previous Coulomb-excitation measurements where possible, and results from lifetime measurements were used if Coulomb-excitation measurements were not available. It was initially assumed that all of the matrix element signs were positive. When creating the **Gosia** input file, matrix element signs were changed to match the mixing ratios given in Ref. [29].

I allowed the matrix elements corresponding to transitions observed in the spectrum in Fig. 4.4 to vary. The exception was the $1/2_1^+ \rightarrow 5/2_1^+$ matrix element, which was used to normalise the other transitions and therefore was fixed. The **Gosia** input included matrix elements from transitions in the literature that were not observed in the data. I also included matrix elements for unobserved but allowed $E2$ transitions. Coulomb-excitation population paths can include population transitions between states that have a highly-inhibited decay transition. While not observed as decay transitions, the population transitions still influence the population of the excited states, and by extension the fitted yields. Therefore, when creating the **Gosia** input file, I added matrix elements for every $E2$ transition allowed by the multipolarity selection rules from Section 2.2.1, as Coulomb excitation populates states via $E2$ transitions. The matrix elements for the unobserved

transitions were calculated using the state mean lifetimes listed in Ref. [29] and were not allowed to vary.

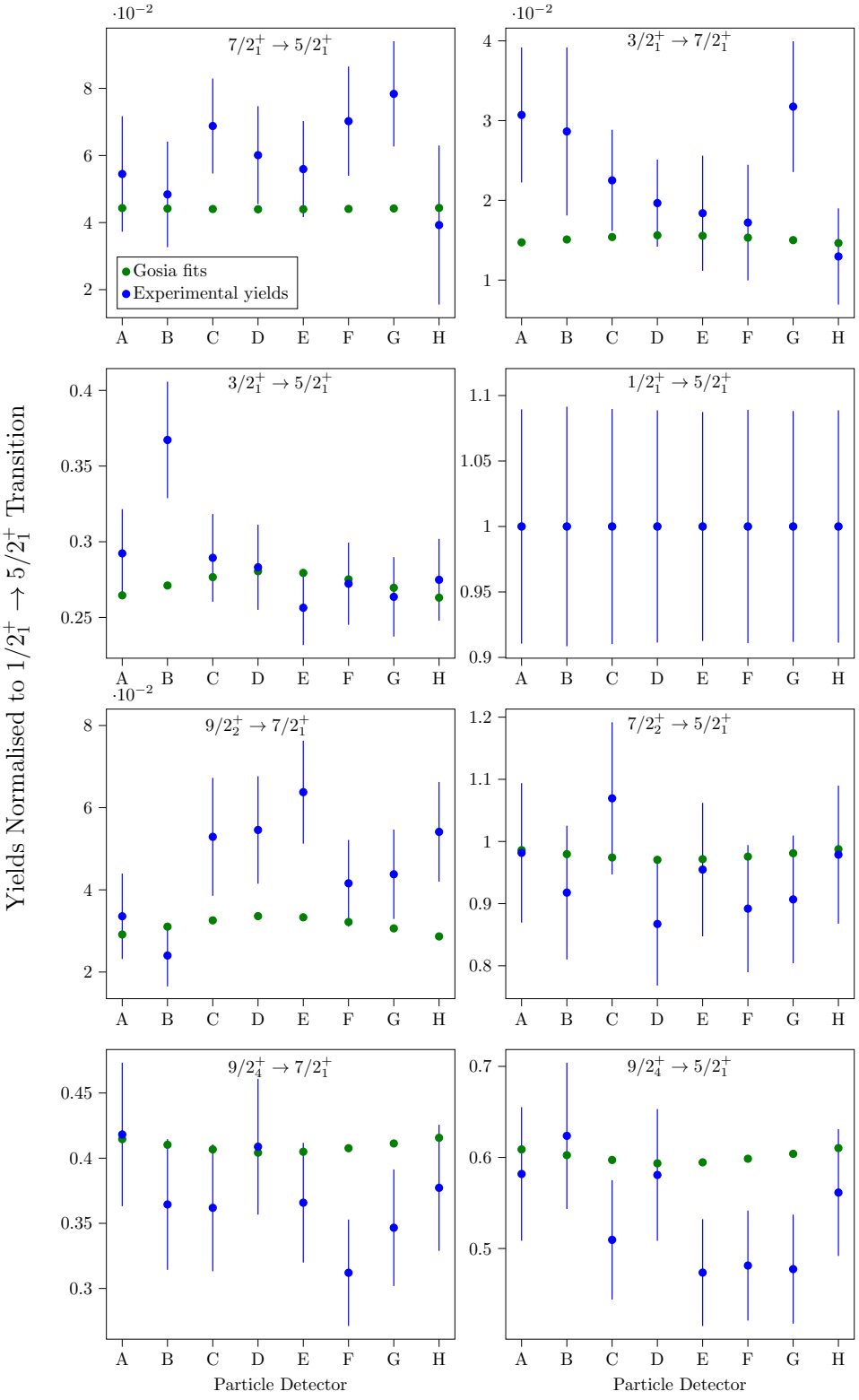

Figure 5.3: The experimental yields of each transition compared to the yields generated by the **Gosia** fits. All yields are normalised to the $1/2_1^+ \to 5/2_1^+$ transition.

5.4.3 Fitted Yields

The fitting process revealed certain relationships between transitions and how the yields were influenced by the population of other excited states. Most of the transition yields were sensitive to changes of the $\langle 9/2_4^+||m(E2)||7/2_1^+\rangle$ matrix element. For some states, they were more sensitive to the $\langle 9/2_4^+||m(E2)||7/2_1^+\rangle$ matrix element than they were to a transition connected to that state. This made sense for the $9/2_4^+ \rightarrow 5/2_1^+$ transition, as both depopulate the $9/2_4^+$ excited state and therefore both vary to maintain the branching ratio between the two transitions. This also made sense for the $7/2_1^+ \rightarrow 5/2_1^+$ transition as the initial state is populated by the $9/2_4^+ \rightarrow 7/2_1^+$ transition. However, the $9/2_2^+ \rightarrow 7/2_1^+$ transition was also highly sensitive to the $\langle 9/2_4^+||m(E2)||7/2_1^+\rangle$ matrix element. This suggested that both the $9/2_2^+$ and $9/2_4^+$ excited states were being populated through the $7/2_1^+$ isomer. Thus, changing the matrix element of a transition to the $9/2_4^+$ would influence the population of the $7/2_1^+$ and $9/2_2^+$ states.

Another influential factor in the fits was the mixing ratio of the mixed transitions. As discussed in Section 2.2.1, some transitions have significant contributions from more than one multipole during γ decay. The low-energy transitions of ^{121}Sb include transitions with notable contributions from both the $M1$ and $E2$ multipoles. The mixing ratio input into **Gosia** was the $E2$ transition probability divided by the $M1$ transition probability. **Gosia** calculated the mixing ratios when performing the fits and compared the calculated mixing ratios to the expected values obtained from Ref. [29]. The fits had a lower χ^2 parameter if the mixing ratio calculated from the fitted matrix elements was within uncertainties of the expected ratio. Similarly, the branching ratio also represented the quality of the fits. The branching ratio is the ratio of intensities of two transitions that decay from the same state. **Gosia** calculated the branching ratios from the fits and an indicator of a poor fit were branching ratios that were well outside uncertainties of the expected values.

The signs of the matrix elements represent the matrix element phase and as a result, the matrix elements interfere with one another while populating and de-populating excited states. This interference contributes to the value of the fitted γ-ray yields. Therefore, switching the sign of the matrix elements changes the interference pattern, and by extent the fitted yields. As discussed in Section 4.4.2, the output represents the local

minimum of the χ^2 parameter of the fit. The yields affect the initial χ^2 value, which shifts the χ^2 local minimum. The fitted matrix element signs matched the sign of the input matrix element because the χ^2 parameter has a large peak at $\chi^2 = 0$. Therefore, the fitting process could not change the sign, which meant the initial signs would influence the local minimum of the χ^2 parameter.

Fig. 5.3 shows the yield ratios for the **Gosia** fits and the experimental yields normalised to the $1/2_1^+ \rightarrow 5/2_1^+$ transition. Approximately half of the **Gosia** yields agree within uncertainty of the experimental yields and all of the **Gosia** fits are within 3σ of the experimental yields. The quality of the fits varied across the transitions but the quality tended to be higher for the transitions with the largest peak areas. The highest-quality fit was the $7/2_2^+ \rightarrow 5/2_1^+$ transition as all but one of the fits aligned within the experimental yield uncertainties. This corresponds to the peak with the highest yields of the seven being considered. Similarly the peak with the worst fit, the $9/2_2^+ \rightarrow 7/2_1^+$ transition, had the lowest yields. While there was not a direct correlation between number of yields and fit quality, it demonstrates the importance of statistics in the quality of the measurements.

Transition	Energy (keV)	$E2$ matrix element (eb)	$B(E2)$ (e^2b^2)	$B(E2)$ (W.u.)
$3/2_1^+ \rightarrow 7/2_1^+$	470	0.808(15)	0.163(5)	45.9(14)
$3/2_1^+ \rightarrow 5/2_1^+$	507	−0.240(5)	0.0143(5)	4.05(14)
$7/2_2^+ \rightarrow 5/2_1^+$	1024	0.801(20)	0.080(4)	22.6(11)
$9/2_2^+ \rightarrow 7/2_1^+$	998	-0.062^{+56}_{-177}	0.0004^{+7}_{-20}	0.108^{+197}_{-563}
$9/2_4^+ \rightarrow 7/2_1^+$	1107	−0.730(30)	0.058(4)	16.3(11)
$9/2_4^+ \rightarrow 5/2_1^+$	1144	-0.930^{+20}_{-10}	0.087^{+4}_{-2}	24.4^{+11}_{-6}

Table 5.1: Fitted reduced matrix elements in ^{121}Sb and the corresponding $B(E2)$ values. Note that the matrix element errors are diagonal errors and have not been correlated. The $7/2_1^+ \rightarrow 5/2_1^+$ transition was an $M1$ transition and the $1/2_1^+ \rightarrow 5/2_1^+$ transition was used for normalisation, so neither had a fitted $E2$ matrix element.

	$B(E2)$ (W.u.)			
Transition	Present work	Adopted Coulomb excitation [29, 61–64]	Hooper *et al.* [64]	Adopted lifetimes [29]
$3/2_1^+ \rightarrow 7/2_1^+$	45.9(14)		0.79(14)	26.0(30)
$3/2_1^+ \rightarrow 5/2_1^+$	4.05(14)	4.14(50)	4.23(12)	4.2(8)
$7/2_2^+ \rightarrow 5/2_1^+$	22.6(11)	15.2(22)	21.1(42)	15.0(40)
$9/2_2^+ \rightarrow 7/2_1^+$	0.108^{+197}_{-563}		1.01(11)	
$9/2_4^+ \rightarrow 7/2_1^+$	16.3(11)			4.0(30)
$9/2_4^+ \rightarrow 5/2_1^+$	24.4^{+11}_{-6}	17.7(62)		

Table 5.2: Summary of the measured $B(E2)$ values compared to other experiments. The adopted Coulomb-excitation values were a weighted average of the results of various Coulomb excitation experiments on ^{121}Sb performed by the author of Ref. [29]. The results from Ref. [64] were included in the weighted average but also measured $B(E2)$ values that were not given in Ref. [29].

5.5 Reduced Matrix Elements and Transition Probabilities

The fitted matrix elements and $B(E2)$ values along with uncertainties are listed in Table 5.1. The comparisons of the experimental $B(E2)$ values to the literature values are listed in Table 5.2. The accuracy of the $B(E2)$ results varies significantly by transition. The $B(E2; 3/2_1^+ \rightarrow 5/2_1^+)$ value agreed within uncertainties for all three literature values and the $B(E2; 9/2_4^+ \rightarrow 5/2_1^+)$ value agreed within uncertainty of the weighted average in Ref. [29]. The $B(E2; 7/2_2^+ \rightarrow 5/2_1^+)$ value agreed within uncertainty of the result in Ref. [64] and was within 2σ of the other literature values. The three other $B(E2)$ values were well outside uncertainty of the literature values. The $B(E2; 9/2_2^+ \rightarrow 7/2_1^+)$ and $B(E2; 9/2_4^+ \rightarrow 7/2_1^+)$ values were over an order of magnitude outside the literature. The $B(E2; 3/2_2^+ \rightarrow 7/2_1^+)$ values showed the most variance across the experimental and literature values. My value and the value calculated from lifetime measurements in the literature did not agree within uncertainties but were within the same order of magnitude. The value from Ref. [64] was two orders of magnitude below the other values for $B(E2; 3/2_2^+ \rightarrow 7/2_1^+)$. A pattern in the results was that the $B(E2)$ values that were well outside literature uncertainties decayed to the $7/2_1^+$ isomer while the $B(E2)$ values that aligned with the literature decayed to the ground state. Additional experimentation is

required to investigate this phenomenon.

A possible explanation is that the data I was fitting was under constrained. Part of the process of measuring γ-ray yields is constraining the data based on known information, thereby ensuring the data aligns with existing results. If the data is under-constrained, then it is less likely to agree with previous results. The source of the under-constrained data could be from a range of factors such as the precision of the particle detectors. Further investigation is needed to see whether the data can be constrained in the analysis to produce $B(E2)$ values that align with the literature.

5.5.1 Lifetimes

Excited state	Energy (keV)	Calculated lifetime (ps)	Adopted lifetime [29] (ps)
$7/2_1^+$	37	4.99×10^3	$4.99(4) \times 10^3$
$3/2_1^+$	507	1.59	2.78(27)
$1/2_1^+$	573	9.57	14.4(23)
$7/2_2^+$	1024	0.111	0.230(40)
$9/2_4^+$	1144	0.287	0.660(130)

Table 5.3: State mean lifetimes calculated from the **Gosia** fits compared to literature values from Ref. [29].

Gosia calculated mean lifetimes for each of the states from the matrix elements, which were compared to the literature lifetimes, as listed in Table 5.3. Only the $7/2_1^+$ isomer mean lifetime was reproduced within uncertainties of the literature values by the **Gosia** fits. The other lifetimes were within an order of magnitude of the literature values but significantly outside uncertainties. I varied the $\langle 7/2_2^+||m(E2)||5/2_1^+\rangle$ matrix element in the input file to examine the influence of the initial matrix element on the calculated mean lifetime. However, varying the $\langle 7/2_2^+||m(E2)||5/2_1^+\rangle$ matrix element had a negligible effect on the calculated lifetime. This further indicated that the data recorded in the experiment was under-constrained, as if the source of the lifetime disparity was the **Gosia** fit, varying the matrix element would have changed the calculated mean lifetime.

Chapter 6

Conclusions

We have successfully conducted experiments to investigate the theoretical assumptions of Coulomb excitation at low energies. I was able to access the low-lying excited states of ^{121}Sb and measure the γ rays emitted during de-excitation in order to calculate the $B(E2)$ values for the transitions and the mean lifetimes of the excited states.

The measurements of the $B(E2 : 3/2_1^+ \rightarrow 5/2_1^+)$, $B(E2 : 7/2_2^+ \rightarrow 5/2_1^+)$ and $B(E2 : 9/2_4^+ \rightarrow 5/2_1^+)$ values agreed within uncertainties with the adopted values from the literature. However, the $B(E2 : 9/2_2^+ \rightarrow 7/2_1^+)$, $B(E2 : 9/2_4^+ \rightarrow 7/2_1^+)$ and $B(E2 : 3/2_1^+ \rightarrow 7/2_1^+)$ values significantly diverged from the literature values by over an order of magnitude. Furthermore, aside from the $7/2_1^+$ isomer, the mean state lifetimes calculated by **Gosia** from the matrix elements were outside uncertainties of the literature lifetime values.

The results highlighted issues with the ability of CAESAR to apply the necessary constraints to the data. The constraints on the data are planned to be improved by installing new particle detectors in CAESAR at HIAF and repeating the experiment. The new detectors will have smaller solid angles that decreases the range of angles at which the data is integrated over, which should improve the precision of the experiment.

The results also demonstrated that the $B(E2)$ values of transitions to the $7/2_1^+$ isomer substantially disagreed with the literature values. Further research is required to determine the cause of this disagreement and if it is related to the under-constraint of the data.

A future goal is to verify the results using a a lower-Z beam. The use of beam species such as protons with $Z = 1$ means that the safe energy will be lower compared to an ^{16}O beam. This decreases the chance that higher-energy states will be accessed, allowing for more focus in the analysis on the low-lying excited states.

An alternative research pathway is to use higher-Z beams to increase the amount of excitation. The magnitude of the excitation in Coulomb excitation is proportional to the charge of the beam nuclei. Beams with higher charge could increase the amount of excitation that occurs. This is because there is more charge in the interaction and therefore the reaction rate is greater [38]. While ^{16}O is a suitable beam for its configuration of excited states, it has a relatively low charge of $Z = 8$. The higher-Z beam will increase the excitation of the low-energy states and produce greater quantities of data to analyse. A potential beam species is ^{28}Si as it has a charge number of $Z = 14$. Additionally, its lowest-energy excited state is at 1779 keV, so it does not overlap with the low-lying ^{121}Sb excited states [65]. Silicon-28 has already been used in Coulomb-excitation experiments at HIAF, so it is a viable beam species for future research into low-energy Coulomb excitation.

Bibliography

[1] M. A. Prelas, C. L. Weaver, M. L. Watermann, E. D. Lukosi, R. J. Schott, and D. A. Wisniewski. "A Review of Nuclear Batteries". *Progress in Nuclear Energy* 75 (2014), pp. 117–148.

[2] G. J. May, A. Davidson, and B. Monahov. "Lead Batteries for Utility Energy Storage: A Review". *Journal of Energy Storage* 15 (2017), pp. 145–157.

[3] T. Yamaguchi, H. Koura, Yu. A. Litvinov, and M. Wang. "Masses of Exotic Nuclei". *Progress in Particle and Nuclear Physics* 120 (2021), p. 103882.

[4] H. A. Bethe and R. F. Bacher. "Nuclear Physics A. Stationary States of Nuclei". *Reviews of Modern Physics* 8.2 (1936), pp. 82–229.

[5] J. Tian, D. Yuan, Y. Cui, Y. Huang, and N. Wang. "Nuclear Mass Parabola and Its Applications". *Chinese Physics C* 43.12 (2019), p. 124104.

[6] M. S. Litz and G. Merkel. *Controlled Extraction Of Energy From Nuclear Isomers*. Tech. rep. Army Research Laboratory, SEDD, DEPG Adelphi, MD 20783: United States Army, 2004.

[7] M. Donya, M. Radford, A. El Guindy, D. Firmin, and M. H. Yacoub. "Radiation in Medicine: Origins, Risks and Aspirations". *Global Cardiology Science and Practice* 2014.4 (2014), p. 57.

[8] P. M. Walker, A. K. Jain, and B. Maheshwari. "Nuclear Isomers". *European Physical Journal Special Topics* 233.5 (2024), pp. 889–892.

[9] G. D. Dracoulis, P. M. Walker, and F. G. Kondev. "Review of Metastable States in Heavy Nuclei". *Reports on Progress in Physics* 79.7 (2016), p. 076301.

[10] A. Bohr. "Rotational Motion in Nuclei". *Reviews of Modern Physics* 48.3 (1976), pp. 365–374.

[11] P. Walker and G. Dracoulis. “Energy Traps in Atomic Nuclei”. *Nature* 399.6731 (1999), pp. 35–40.

[12] C. J. Chiara, J. J. Carroll, M. P. Carpenter, J. P. Greene, D. J. Hartley, R. V. F. Janssens, G. J. Lane, J. C. Marsh, D. A. Matters, M. Polasik, J. Rzadkiewicz, D. Seweryniak, S. Zhu, S. Bottoni, A. B. Hayes, and S. A. Karamian. “Isomer Depletion as Experimental Evidence of Nuclear Excitation by Electron Capture”. *Nature* 554.7691 (2018), pp. 216–218.

[13] Y. Wang, Z. Ma, Y. Yang, C. Fu, W. He, and Y. Ma. “Feasibility Study of Nuclear Excitation by Electron Capture Using an Electron Beam Ion Trap”. *Frontiers in Physics* 11 (2023).

[14] K. S. Krane and D. Halliday. *Introductory Nuclear Physics*. New York: Wiley, 1987.

[15] A. E. Stuchbery and J. L. Wood. “To Shell Model, or Not to Shell Model, That Is the Question”. *Physics* 4.3 (2022), pp. 697–773.

[16] M. G. Mayer. “On Closed Shells in Nuclei”. *Physical Review* 74.3 (1948), pp. 235–239.

[17] M. G. Mayer. “On Closed Shells in Nuclei. II”. *Physical Review* 75.12 (1949), pp. 1969–1970.

[18] G. F. Bertsch. “Vibrations of the Atomic Nucleus”. *Scientific American* 248.5 (1983), pp. 62–73.

[19] H. C. Pauli, K. Alder, and R. M. Steffen. “The Theory of Internal Conversion”. In: *The Electromagnetic Interaction in Nuclear Spectroscopy*. Ed. by W. D. Hamilton. Amsterdam : New York: North-Holland ; American Elsevier, 1975, pp. 341–440.

[20] K. Alder and R. M. Steffen. “Emission and Absorption of Electromagnetic Radiation”. In: *The Electromagnetic Interaction in Nuclear Spectroscopy*. Ed. by W. D. Hamilton. Amsterdam : New York: North-Holland ; American Elsevier, 1975, pp. 1–38.

[21] K. Alder and R. M. Steffen. “Emissions of Gamma Radiation and Nuclear Structure”. In: *The Electromagnetic Interaction in Nuclear Spectroscopy*. Ed. by W. D. Hamilton. Amsterdam : New York: North-Holland ; American Elsevier, 1975, pp. 39–54.

[22] J.O. Newton. “Coulomb Excitation”. In: *The Electromagnetic Interaction in Nuclear Spectroscopy*. Ed. by W. D. Hamilton. Amsterdam : New York: North-Holland ; American Elsevier, 1975, pp. 237–285.

[23] A. B. Hayes, D. Cline, C. Y. Wu, M. W. Simon, R. Teng, J. Gerl, Ch. Schlegel, H. J. Wollersheim, A. O. Macchiavelli, K. Vetter, P. Napiorkowski, and J. Srebrny. “Coulomb Excitation Paths of High-K Isomer Bands in 178Hf”. *Physical Review Letters* 89.24 (2002), p. 242501.

[24] S. Leoni, B. Fornal, N. Mărginean, and J. N. Wilson. “Shape Isomers: Status and Perspectives across the Nuclear Chart”. *European Physical Journal Specical Topics* 233.5 (2024), pp. 1061–1074.

[25] V. Metag, D. Habs, and H. J. Specht. “Spectroscopic Properties of Fission Isomers”. *Physics Reports* 65.1 (1980), pp. 1–41.

[26] A. K. Jain, B. Maheshwari, S. Garg, M. Patial, and B. Singh. “Atlas of Nuclear Isomers”. *Nuclear Data Sheets* 128 (2015), pp. 1–130.

[27] T. Otsuka, T. Suzuki, R. Fujimoto, H. Grawe, and Y. Akaishi. “Evolution of Nuclear Shells Due to the Tensor Force”. *Physical Review Letters* 95.23 (2005), p. 232502.

[28] A. J. Mitchell. “Investigating High-j Single-Particle Energies in Z = 51 Nuclei”. PhD Diss. Manchester: University of Manchester, 2012.

[29] S. Ohya. “Nuclear Data Sheets for A = 121”. *Nuclear Data Sheets* 111.6 (2010), pp. 1619–1806.

[30] J. Blachot. “Nuclear Data Sheets for A = 117”. *Nuclear Data Sheets* 95.3 (2002), pp. 679–836.

[31] D. M. Symochko, E. Browne, and J. K. Tuli. “Nuclear Data Sheets for A = 119”. *Nuclear Data Sheets* 110.11 (2009), pp. 2945–3105.

[32] J. Chen. “Nuclear Data Sheets for A = 123”. *Nuclear Data Sheets* 174 (2021), pp. 1–463.

[33] J. Katakura. “Nuclear Data Sheets for A = 125”. *Nuclear Data Sheets* 112.3 (2011), pp. 495–705.

[34] A. Hashizume. “Nuclear Data Sheets for A = 127”. *Nuclear Data Sheets* 112.7 (2011), pp. 1647–1831.

[35] D. Cline. “Nuclear Shapes Studied by Coulomb Excitation”. In: *Nuclear Structure 1985*. Elsevier, 1985, pp. 313–326.

[36] M. Rocchini and M. Zielińska. “Low-Energy Coulomb Excitation for the Shell Model”. *Physics* 3.4 (2021), pp. 1237–1253.

[37] J. M. Cook, T. Glasmacher, and A. Gade. “Accuracy of B(E2 ; 0ˆ+_1 → 2ˆ+_1) Transition Rates from Intermediate-Energy Coulomb Excitation Experiments”. *Physical Review C* 73.2 (2006), p. 024315.

[38] D. Cline, T. Czosnyka, A. B. Hayes, P. Napiorkowski, N. Warr, and C. Y. Wu. *GOSIA User Manual for Simulation and Analysis of Coulomb Excitation Experiments*. 2012.

[39] K. Buchtela. “Radiochemical Methods | Gamma-Ray Spectrometry”. In: *Encyclopedia of Analytical Science*. Elsevier, 2005, pp. 72–79.

[40] J. H. L. Mott and J. M. Daniel. “Interactions of Electromagnetic Radiation and Subatomic Particles with Matter – Part 1”. *Clinical Oncology* 33.7 (2021), pp. 451–454.

[41] G. F. Knoll. *Radiation Detection and Measurement*. 4th ed. Hoboken, N.J: John Wiley, 2010.

[42] M. P. Carpenter, T. L. Khoo, I. Ahmad, R. V. F. Janssens, T. Lauritsen, G.A. Annan, A.M. Baxter, M.E. Bleich, S. Harfenist, E.F. Moore, M. Torelli, and D.W. Visser. “Test and Performance of a BGO Compton-suppression Shield for GAMMASPHERE”. *Nuclear Instruments and Methods in Physics Research Section A: Accelerators, Spectrometers, Detectors and Associated Equipment* 353.1-3 (1994), pp. 234–238.

[43] V. Selamneni and P. Sahatiya. "Mixed Dimensional Transition Metal Dichalcogenides (TMDs) vdW Heterostructure Based Photodetectors: A Review". *Microelectronic Engineering* 269 (2023), p. 111926.

[44] XIA. *Pixie-16 User Manual*. 3rd ed. USA: XIA LLC, 2019.

[45] D. R. Tilley, H. R. Weller, and C. M. Cheves. "Energy Levels of Light Nuclei A = 16–17". *Nuclear Physics A* 564.1 (1993), pp. 1–183.

[46] T.R. Ophel, J.S. Harrison, J.O. Newton, R.H. Spear, E.W. Titterton, and D.C. Weisser. "The 14UD Pelletron Accelerator at the Australian National University". *Nuclear Instruments and Methods* 122 (1974), pp. 227–234.

[47] Rene Brun and Fons Rademakers. "ROOT — An Object Oriented Data Analysis Framework". *Nuclear Instruments and Methods in Physics Research Section A: Accelerators, Spectrometers, Detectors and Associated Equipment* 389.1-2 (1997), pp. 81–86.

[48] M.-M. Bé, V. Chisté, C. Dulieu, E. Browne, V. Chechev, N. Kuzmenko, R. Helmer, A. Nichols, E. Schönfeld, and R. Dersch. *Table of Radionuclides*. Vol. 2. Monographie BIPM-5. Pavillon de Breteuil, F-92310 Sèvres, France: Bureau International des Poids et Mesures, 2004.

[49] P. Doornenbal. "In-Beam Gamma-Ray Spectroscopy at the RIBF". *Progress of Theoretical and Experimental Physics* 2012.1 (2012).

[50] P. H. Regan. *RADWARE on the ANU VAX System*. Technical Report ANU-P-1176. Canberra: Australian National University, 1994.

[51] M.-M. Bé, V. Chisté, C. Dulieu, X. Mougeot, E. Browne, V. Chechev, N. Kuzmenko, F. Kondev, A. Luca, M. Galán, A. L. Nichols, A. Arinc, and X. Huang. *Table of Radionuclides*. Vol. 5. Monographie BIPM-5. Pavillon de Breteuil, F-92310 Sèvres, France: Bureau International des Poids et Mesures, 2010.

[52] M.-M. Bé, V. Chisté, C. Dulieu, M. A. Kellett, X. Mougeot, A. Arinc, V. P. Chechev, N. K. Kuzmenko, T. Kibédi, A. Luca, and A. L. Nichols. *Table of Radionuclides*. Vol. 8. Monographie BIPM-5. Pavillon de Breteuil, F-92310 Sèvres, France: Bureau International des Poids et Mesures, 2016.

[53] B. A. De Luna and D. A. Haas. “Gamma-Gamma Coincidence Spectroscopy Analysis with Cascade Summing Corrections in Close Counting Geometries”. *Nuclear Instruments and Methods in Physics Research Section A: Accelerators, Spectrometers, Detectors and Associated Equipment* 1065 (2024), p. 169468.

[54] K. Alder and A. Winther. *Electromagnetic Excitation: Theory of Coulomb Excitation with Heavy Ions*. Amsterdam: North-Holland Publ., 1975.

[55] H. Morinaga and T. Yamazaki. *In-Beam Gamma-Ray Spectroscopy*. Amsterdam New York: North-Holland Pub. Co, 1976.

[56] T. Tamura, H. Iimura, K. Miyano, and S. Ohya. “Nuclear Data Sheets for A = 121”. *Nuclear Data Sheets* 64 (1991), pp. 323–428.

[57] A. Abragam and R. V. Pound. “Influence of Electric and Magnetic Fields on Angular Correlations”. *Physical Review* 92.4 (1953), pp. 943–962.

[58] K. Alder and A. Winther. *Coulomb Excitation: A Collection of Reprints*. Perspectives in Physics. Academic Press, 1966.

[59] T. Kibédi, T.W. Burrows, M.B. Trzhaskovskaya, P.M. Davidson, and C.W. Nestor. “Evaluation of Theoretical Conversion Coefficients Using BrIcc”. *Nuclear Instruments and Methods in Physics Research Section A: Accelerators, Spectrometers, Detectors and Associated Equipment* 589.2 (2008), pp. 202–229.

[60] J. F. Ziegler, M. D. Ziegler, and J. P. Biersack. “SRIM – The Stopping and Range of Ions in Matter (2010)”. *Nuclear Instruments and Methods in Physics Research Section B: Beam Interactions with Materials and Atoms* 268.11-12 (2010), pp. 1818–1823.

[61] M. F. Thomas and M. A. Grace. “Coulomb Excitation of Low-Energy States in 127I, 121Sb and 183W”. *Nuclear Physics* 88.1 (1966), pp. 56–62.

[62] K. C. Jain, K. P. Singh, G. Singh, S. S. Datta, and I. M. Govil. “Coulomb Excitation Studies in Antimony Isotopes”. *Physical Review C* 40.5 (1989), pp. 2400–2402.

[63] P.D. Barnes, C. Ellegaard, B. Herskind, and M.C. Joshi. “Properties of Levels in 121Sb and 123Sb Excited with the Reactions (3He, d), (d, d’) and (16O, 16O’λ)”. *Physics Letters* 23.4 (1966), pp. 266–269.

[64] H. R. Hooper, P. W. Green, H. E. Siefken, G. C. Neilson, W. J. McDonald, D. M. Sheppard, and W. K. Dawson. “Energy Levels below 2 MeV in Sb 121 and Sb 123”. *Physical Review C* 20.6 (1979), pp. 2041–2051.

[65] M. Shamsuzzoha Basunia. “Nuclear Data Sheets for A = 28”. *Nuclear Data Sheets* 114.10 (2013), pp. 1189–1291.